Supplement of The Cryosphere, 20, 1895–1928, 2026
https://doi.org/10.5194/tc-20-1895-2026-supplement

The Cryosphere Open Access EGU

Supplement of

DCG-MIP: the Debris-Covered Glacier melt Model Intercomparison exPeriment

Francesca Pellicciotti et al.

Correspondence to: Francesca Pellicciotti (francesca.pellicciotti@ista.ac.at) and Adrià Fontrodona-Bach (adria.fontrodona-bach@ista.ac.at)

1. Study sites and data

Table S1. Debris properties at the sites. Source indicates if the property was directly measured in the field, derived from field measurements, optimised, or assumed (i.e. taken from the literature).

Site	Surface roughness, z_0 (m)			Thermal conductivity, k (W m^{-1}K^{-1})		
	Value	Uncertainty	Source	Value	Uncertainty	Source
Arolla	0.0160	0.0010	Assumed - Brock et al. (2010)	0.96	0.10	Assumed - Brock et al. (2010)
Changri Nup	0.0500	0.005–0.5	Optimised - Lejeune et al. (2013)	0.70	0.10	Optimised - Lejeune et al. (2013)
Djankuat	0.0160	0.0008	Assumed - Bozhinsky (1986)	2.80	0.10	Assumed - Bozhinsky (1986)
Lirung	0.0350	0.0150	Derived - Miles et al. (2017)	1.55	0.30	Derived - Unpublished
Miage	0.0160	0.0010	Derived - Brock et al. (2010)	1.04	0.07	Derived - Brock et al. (2010)
Piramide	0.0190	0.0019	Derived - McPhee et al. (2019)	0.92	0.09	Assumed - Robertson (1988)
Suldenferner	0.0036	0.0004	Optimised - McCarthy (2018)	0.70	0.07	Derived - McCarthy (2018)
Tapado	0.0200	0.0020	Assumed - McPhee et al. (2019b)	0.94	0.09	Assumed - Brock et al. (2010)
Tasman	0.0160	0.0010	Assumed - Brock et al. (2010)	1.80	0.20	Derived - Röhl (2008)
Site	Porosity, ϕ (-)			Emissivity, ε (-)		
	Value	Uncertainty	Source	Value	Uncertainty	Source
Arolla	0.33	10%	Assumed - Brock et al. (2010)	0.96	1%	Assumed - Carenzo et al. (2016)
Changri Nup	0.37	8%	Measured - Wagnon (2019)	0.95	1%	Optimised - Lejeune et al. (2013)
Djankuat	0.42	12%	Assumed - Bozhinsky (1986)	0.90	5%	Assumed - Bozhinsky (1986)
Lirung	0.29	10%	Measured - Steiner et al. (2021)	0.94	2%	Assumed - Brock et al. (2010)
Miage	0.33	10%	Measured - Brock et al. (2010)	0.94	1%	Derived - Brock et al. (2010)
Piramide	0.33	10%	Assumed - Brock et al. (2010)	0.93	1%	Assumed - Brock et al. (2010)
Suldenferner	0.33	10%	Assumed - Brock et al. (2010)	0.94	1%	Assumed - Brock et al. (2010)
Tapado	0.33	10%	Assumed - Brock et al. (2010)	0.94	1%	Assumed - Brock et al. (2010)
Tasman	0.33	10%	Assumed - Brock et al. (2010)	0.94	2%	Assumed - Brock et al. (2010)

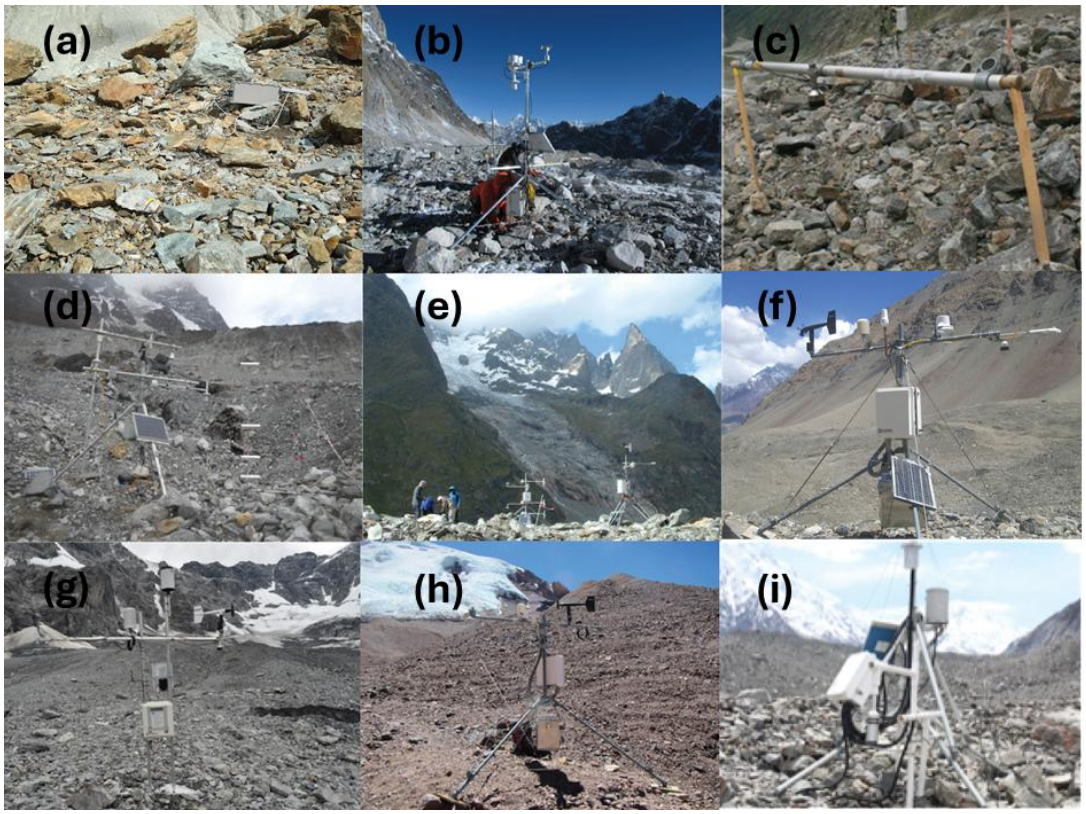

Figure S1. Automatic weather station location at the nine study sites. (a) Arolla; (b) Changri Nup; (c) Djankuat; (d) Lirung; (e) Miage; (f) Piramide; (g) Suldenferner; (h) Tapado; (i) Tasman.

Table S2. Estimates of validation data uncertainty given by data providers for measurements at the UDG, ablation stakes, and for the longwave radiation measurements used to derive surface temperature. Most estimates are the sensor's accuracy, not the actual measurement uncertainty.

Site	UDG / Stakes Uncertainty	Longwave Radiation Uncertainty
Arolla	± 5%	± 10%
Changri Nup	± 5 cm	± 3%
Djankuat	± 1 cm	± 15 W m^{-2}
Lirung	± 5%	± 5%
Miage	± 2 cm (stakes)	± 10%
Pirámide (stakes)	± 2 cm (stakes)	± 5%
Suldenferner	± 1 cm or 0.4%	± 10%
Tapado	± 5%	± 10%
Tasman	± 5%	± 10%

Table S3. Summary of meteorological forcing variables at each site. Mean temperature (T), relative humidity (RH), wind speed (FF), incoming shortwave and longwave radiation ($S\downarrow$, $L\downarrow$), outgoing shortwave radiation ($S\uparrow$), albedo (α, calculated as $S\uparrow$ divided by $S\downarrow$) and sum of precipitation (PP) over the period used for modelling. All means are daily.

Site	T (°C)	RH (%)	FF (m s^{-1})	$S\downarrow$ (W m^{-2})	$S\uparrow$ (W m^{-2})	α (-)	$L\downarrow$ (W m^{-2})	P (mm)
Arolla	5.7	72.8	3.3	190.7	29.8	0.16	294.5	215.2
Changri Nup	-1.4	75.5	1.9	213.5	51.0	0.24	279.7	257.7
Djankuat	7.3	66.7	2.3	267.6	36.6	0.14	289.7	337.3
Lirung	7.1	83.1	0.4	206.6	29.2	0.14	316.3	520.9
Miage	10.8	66.7	2.4	248.1	31.5	0.13	304.7	310.8
Pirámide	5.8	34.5	4.0	259.3	38.9	0.15	255.7	106.2
Suldenferner	6.7	75.1	2.4	199.2	36.7	0.18	301.0	234.6
Tapado	2.3	29.1	2.6	357.6	41.3	0.12	223.2	0.0
Tasman	12.9	57.0	2.8	240.8	21.6	0.09	328.5	1529.8

2. Model descriptions

This section of the supplement provides a small summary of all participating models in the debris-covered glacier melt model intercomparison experiment. An extended summary of all models, using a standard template that was filled in by each modeller, can be found at https://doi.org/10.5281/zenodo.15754455.

As in the main text, the models are sorted and described from more complex to less complex, according to our definition of complexity stated in Section 4 in the main text, and Fig. 3.

2.1. Energy balance models

An overview table of all energy balance models and how each model calculates each flux is presented in Table SI4 below the descriptions.

DEB_{CF}

Most models in this intercomparison experiment are at least partly based on the DEB model (debris energy-balance model) by Reid and Brock (2010), which we therefore describe as first and in more detail than the others. According to our definition of model complexity, the configuration of DEB_{CF} is the most complex of all participating models.

The model was developed first as a point-scale model by Reid and Brock (2010) and then was restructured into a distributed form in Fyffe *et al.* (2014). It calculates the energy balance at the surface of the debris, using the iterative Newton-Raphson method to derive the debris surface temperature. The model used for this experiment is the version used in Fyffe *et al.* (2014).

It is very similar to that in Reid and Brock (2010) but with three changes: 1) a snow component was added to simulate snow melt when snow covers debris; 2) thresholds were added to the Richardson number used to calculate the turbulent heat flux (see below); and 3) the debris is split into 10 layers for the calculation of heat conduction through the debris (so each layer is the debris thickness divided by 10). Changes to parameters resulted from the guidelines of this intercomparison experiment.

At the surface, the model calculates net shortwave radiation (*S*), net longwave radiation (*L*), sensible heat flux (*H*), latent heat flux (*LE*), heat flux due to precipitation (*P*) and the conductive heat flux below the surface (*G*).

$$M = S + L + H + LE + P + G \tag{S1}$$

where *M* is the energy available for ablation of debris-covered ice.

When there were occasional snow falls a simple energy balance snowmelt model was applied, with the general form:

$$a = \frac{\Delta t}{\rho_w L_f}[S + L + H + LE + P] \tag{S2}$$

where here *a* is snow ablation, Δt is the model time step, ρ_w is the water density and L_f is the latent heat of fusion of water. Conduction of heat or penetration of shortwave radiation into the snow was not modelled. The snow surface was assumed to remain at 0°C and the surface relative humidity was assumed to be 100%. Emissivity and surface roughness lengths are given literature values for snow (see Table S7). The calculation of the fluxes was the same as for the debris melt model.

For this experiment, *S* was calculated from the given incoming and outgoing shortwave radiation, rather than prescribing a snow/debris albedo, and if outgoing shortwave radiation was greater than incoming shortwave radiation it was made equal to the incoming shortwave radiation. L was calculated following standard methods outlined in Reid and Brock (2010), i.e. following the Stefan-Boltzmann law.

The turbulent sensible and latent heat fluxes were calculated using the bulk aerodynamic method, using the Richardson number to calculate the stability of the surface layer. For the MMI this was as outlined in Reid and Brock (2010), but with the thresholds on the Richardson number added in Fyffe et al. (2014) so that if $R_b > 0.2$ (turbulence ceased, airflow laminar) or $R_b < -1$ (free convection, conditions very unstable) then $R_b = 0$. For this experiment, if the instrument heights of wind speed and air temperature were different, then the height of the air temperature instrument was used for the sensible heat flux, similarly if the measurement heights of wind speed and relative humidity were different then the height of the relative humidity instrument was used to calculate the latent heat flux. Since no surface relative humidity data were provided it was assumed that the surface relative humidity equaled 100% whenever precipitation occurred. The latent heat flux was therefore only calculated at the timesteps with precipitation. The heat flux due to precipitation was calculated as given in Reid and Brock (2010).

The conductive heat flux, *G*, at the surface of the debris (note not the same as G_i) is approximated using T_s and the temperature of the debris at the first calculation layer, $T_d(1)$:

$$G = K\left(\frac{dT_d}{dz}\right)_{surface} \approx K\frac{T_d(1) - T_s}{h_l} \tag{S3}$$

where h_l is the calculation layer thickness (m), *K* is the debris thermal conductivity (W m^{-1} K^{-1}) and *z* is depth in the debris. Each layer within the debris is the debris thickness divided by 10 (this is the method used in Fyffe *et al.*, 2014). In Reid and Brock (2010) the debris calculation layer thickness was 1 cm unless the cover was thinner than 5 cm, in which case the number of layers was fixed at 5. Either method can easily be implemented in the DEB model. The conductive heat flux which reaches the glacier ice, G_i, depends on the temperature gradient at the base of the debris:

$$G_i(t) = K\left(\frac{dT_d}{dz}\right)_{base} \approx K\frac{T_d(N-1) - T_f}{h_l} \tag{S4}$$

where T_f is the temperature at the ice debris interface, which equals 0 °C. Then the melt beneath the debris (*a*) is calculated from:

$$a = \frac{G_i \Delta t}{\rho_w L_f} \tag{S5}$$

The debris surface temperature, T_s is required for G, and the outgoing longwave radiation, sensible heat flux, latent heat flux and the heat flux due to precipitation, but it is not known. To solve this problem the model solves the energy balance numerically; so that it varies the debris surface temperature until the sum of the heat fluxes at the debris surface is zero, using the iterative Newton-Raphson method:

$$T_s(n+1) = T_s(n) - \frac{F(T_s(n))}{F'(T_s(n))} \quad \text{(S6)}$$

where $F'(T_s)$ is the derivative of the total surface flux with respect to T_s (the debris surface temperature, °C), and is calculated numerically by the central difference method. For each model time step $T_s(n = 0)$ must have an initial value, so for the first time step it is equal to the air temperature, and for further timesteps it is the value from the previous time step. This equation is repeated until $|T_s(n + 1) - T_s(n)| < 0.01$. To calculate the conduction of heat through the debris to the ice/debris interface the following equation is used:

$$\rho_d C_{pd} \frac{\partial T_d(z_d,t)}{\partial t} = \frac{\partial}{\partial z_d}\left(K \frac{\partial T_d(z_d,t)}{\partial z_d}\right) \quad \text{(S7)}$$

which uses the partial derivatives of debris temperature, T_d, with respect to time, t and depth in the debris, z_d (m), where ρ_d is debris density (kg m^{-3}), C_{pd} is the debris specific heat (J kg^{-1} K^{-1}) and K is the debris thermal conductivity (W m^{-1} K^{-1}).

Table S4. Values of physical and empirical parameters used by the DEB model. *From Robinson and Coruh (1988), cited in Brock et al. (2010, p10). **From Lide (2004), cited in Brock et al. (2010, p10). ***From Brock et al. (2006, p288). ****Same as ice emissivity in Reid and Brock (2010). Note that the ice density was changed from 915 kg m^{-3} to 900 kg m^{-3} following the DCG-MIP guidelines.

Parameter	Debris Density* (kg m^{-3})	Density of Ice (kg m^{-3})	Debris Specific Heat Capacity** (J kg^{-1} K^{-1})	Snow Aerodynamic Roughness*** (m)	Snow Emissivity****
All sites	1496	900	948	0.00231	0.97

ROU15

This model is based on Rounce et al. (2015) and calculates the same fluxes at the debris surface as the DEB_{CF} model: S, L, H, LE, P and G. Despite the similarities with DEB_{CF}, it is considered slightly simpler than DEB_{CF} as it assumes neutral conditions in the calculation of the turbulent heat fluxes.

The model has a snowpack module to calculate snow accumulation and melt based on meteorological forcing. However, snow depth was provided as part of the input data, and therefore when there is snow on the surface, the model assumes the net radiation flux, latent heat flux, sensible heat flux, and precipitation heat flux are zero, and only accounts for the ground heat flux and the conductive heat flux at the snow/debris surface interface.

The calculation of the turbulent heat fluxes differs from DEB_{CF}. The sensible heat flux is estimated according to Nicholson and Benn (2006), assuming neutral conditions without stability corrections. The latent heat flux is also estimated according to Nicholson and Benn (2006), with the debris surface assumed to be saturated when it is raining. The precipitation heat flux and the heat conduction through the debris are estimated in the same way as the model DEB_{CF}, both following Reid and Brock (2010), and with the debris layer discretized in 10 layers of equal thickness.

Table S5. Values of physical and empirical parameters used by the ROU15 model.

Parameter	Debris Density* (kg m^{-3})	Density of Ice (kg m^{-3})	Debris Specific Heat Capacity** (J kg^{-1} K^{-1})
All sites	2700	900	750

$GRO17_B$

The theoretical model of glacial melt under a porous debris layer developed by Evatt et al. (2015) provides the basis for the energy balance model GRO17 (Groos et al., 2017; Groos & Mayer, 2017). A main difference compared to earlier models (e.g. Nicholson and Benn, 2006; Reid and Brok, 2010) is the incorporation of the turbulent latent heat flux within the porous debris layer. Due to the treatment of the debris layer as a porous medium and the consideration of evaporation at the debris-ice

interface, the model is able to capture the shape of Østrem curves derived from in-situ measurements (Evatt et al., 2015). Two different model versions, GRO17A and GRO17B, were applied in the model intercomparison experiment: GRO17B assumes a permeable debris layer and accounts for the turbulent latent heat flux within the debris, while GRO17A assumes an impermeable debris layer and accounts only for heat conduction to transfer energy through the debris layer.

For GRO17B, the energy balance at the debris-atmosphere interface is given by

$$Q_D = Q_S + Q_L + Q_{SH} \tag{S8}$$

and at the debris-ice interface by

$$Q_D = Q_M + Q_V \tag{S9}$$

where Q_D is the ground heat flux (W m^{-2}), Q_S is the shortwave energy flux (W m^{-2}), Q_L is the longwave energy flux (W m^{-2}), Q_{SH} is the sensible heat flux (W m^{-2}), Q_M is the latent heat of melting (W m^{-2}) and Q_V is the evaporative (or turbulent latent) heat flux (W m^{-2}) (for a detailed description and derivation of the individual fluxes see equations 1, 2, 5, 6, 29 and 31 in Evatt et al., 2015).

The model could theoretically manage the snow cover on top of the debris using a simple temperature index approach, but for simplicity and consistency, sub-debris ice melt was set to zero if the height of the snow cover was >0.0 m.

In contrast to the other participating energy balance models, the GRO17B model would require additional parameters like friction velocity (u_*), debris porosity (phi) and grain size to describe the geometry of the porous debris layer. These properties determine the wind speed attenuation parameter (γ) that controls the decay of the airflow through the debris layer (see equations 23 and 52 in Evatt et al., 2015). However, information on grain size was not available and porosity was not measured at most sites (see Table S1). Therefore, the wind speed attenuation constant (γ) was calibrated by minimising the difference (RMSE) between Q_{SH} modelled by Eq. 31 from Evatt et al. (2015) and Q_{SH} modelled by Eq. 7 from Nicholson and Benn (2006). Similarly, the friction velocity (u_*), required for the calculation of the sensible heat flux is parameterised as $u_* = u_m / \alpha$, where u_m is the measured wind speed and α is a scaling factor calibrated by minimising the difference (RMSE) between Q_{SH} modelled by Eq. 32 from Evatt et al. (2015) and Q_{SH} modelled by Eq. 7 from Nicholson and Benn (2006).

The downward heat flux through the debris is modelled by Fourier's law, assuming a linear temperature profile derived from the quasi steady-state heat equation (see Evatt et al., 2015). For the calculation of the internal temperature profile, the debris layer was discretised into n layers of 1 cm thickness.

Solving the heat conduction through the debris in a quasi steady state makes this model simpler than DEBCF and ROU15, despite the added complexity of this model with regards to solving the latent heat flux within the porous debris layer. GRO17 is the only model which takes into account a fraction of debris embedded in the ice when calculating ice melt under debris from the conductive heat flux reaching the ice.

Table S6. Summary of parameter values for GRO17$_B$ sites, including friction velocity (u^*), wind speed attenuation constant (γ), ice density (ρ_i), volume fraction of debris (θ_d), and measurement height. u_m is the mean wind speed at the site.

Site	u^* (m/s)	γ	ρ_i (kg/m^3)	θ_d	Height (m)
Arolla	$u_m/12.1$	67	900	0.01	2
Changri Nup	$u_m/9.2$	20	900	0.01	2
Djankuat	$u_m/12.0$	82	900	0.01	2
Lirung	$u_m/9.8$	47	900	0.01	2
Miage	$u_m/12.0$	67	900	0.01	2
Piramide	$u_m/11.6$	49	900	0.01	2
Suldenferner	$u_m/15.7$	308	900	0.01	2
Tapado	$u_m/11.5$	52	900	0.01	2
Tasman	$u_m/12.1$	52	900	0.01	2

d2EB

This model is based on Steiner et al. (2018, 2021) and calculates the following fluxes: *S*, *L*, *H*, *LE* and *G*.

In general, the model is simply Reid and Brock (2010) with the only adaptation that turbulent fluxes are calculated based on Steiner et al. (2018, 2021) and Nicholson and Benn (2006). This was done according to Steiner et al. as the parametrization with the Richardson number fails on debris due to the strong heating. The model does not deal with snow.

The sensible heat flux is calculated following Equation 1 and 4 in Steiner et al. (2018) and assuming neutral stability over the debris cover as in Nicholson and Benn (2006). The latent heat flux is calculated following Equations 2 and 4 in Steiner et al. (2018). The model requires specific humidity but is calculated from standard formulas for relative humidity and saturation vapour pressure as a function of temperature.

Heat conduction through the debris is calculated as in Reid and Brock (2010) and the number of debris layers is a function of the thickness (N = thickness [m] / 0.01).

Table S7. Values of physical and empirical parameters used by the d2EB model.

Parameter	Debris Density (kg m^{-3})	Density of Ice (kg m^{-3})	Specific Heat Capacity of Debris (J kg^{-1} K^{-1})
All sites	2650	900	890

DEB_{PG}

This model is the same as DEB_{CF} described above, except for the following differences:

- DEB_{PG} does not deal with snow, so it does not calculate snow accumulation and melt on top of the debris.
- DEB_{PG} does not calculate the precipitation heat flux and therefore does not need precipitation as input data.
- DEB_{PG} calculates the latent heat flux when the relative humidity of the surface is 100% and assumes that is the case when the relative humidity of the air is 100%.
- DEB_{PG} has a different debris layer discretisation than DEB_{CF}. For debris thickness less than 6 cm, d/3 layers assumed. For debris thickness more than 6 cm, each calculation layer was 2-2.05 cm thick.

Table S8. Values of physical and empirical parameters used by the DEBGA model. *From Robinson and Coruh (1988), cited in Brock et al. (2010, p10).

Parameter	Debris Density* (kg m^{-3})	Density of Ice (kg m^{-3})	Debris Specific Heat Capacity* (J kg^{-1} K^{-1})
All sites	1496	900	948

$GRO17_A$

This model is the same as GRO17B described above, except that GRO17A assumes a permeable debris layer and therefore has the following two differences in model configuration:

- GRO17A disregards the evaporation heat flux (Q_V).
- GRO17A expresses the sensible heat flux analogue to previous studies (e.g. Nicholson and Benn, 2006; as in equation 32 in Evatt et al., 2015).

Table S9. Summary of parameter values for GRO17A sites, including friction velocity (u^*), ice density (ρ_i), volume fraction of debris (Φ), and measurement height. u_m is the mean wind speed at the site.

Site	u^* (m/s)	ρ_i (kg/m^3)	Φ	Height (m)
Arolla	$u_m/12.1$	900	0.01	2
Changri Nup	$u_m/9.2$	900	0.01	2
Djankuat	$u_m/12.0$	900	0.01	2
Lirung	$u_m/9.8$	900	0.01	2
Miage	$u_m/12.0$	900	0.01	2
Piramide	$u_m/11.6$	900	0.01	2
Suldenferner	$u_m/15.7$	900	0.01	2
Tapado	$u_m/11.5$	900	0.01	2
Tasman	$u_m/12.1$	900	0.01	2

A-Melt

The A-Melt model is a distributed energy-balance model developed for alpine regions of snow and ice melting and meltwater runoff formation (Rets and Kireeva, 2010; Elagina et al., 2025). For this study a simplified 1D version of the model was developed.

The heat balance of the surface of snow or debris is defined at every time step as:

$$\omega = S_{\text{down}} - S_{\text{out}} + E_{\text{lrd}} - E_{\text{lu}} \pm LE \pm H \pm Q_m \pm Q_{\text{act}} \quad \text{(S10)}$$

where ω is the net energy flux on the surface, W m^{-2}; S_{down} is the downward shortwave radiation flux, W m^{-2}; Sout is an upward shortwave radiation flux, W m^{-2}; E_{lru} is outgoing long-wave radiation, W m^{-2}; E_{lrd} is the counter radiation of the atmosphere, W m^{-2}; LE is the turbulent latent heat flux density, W m^{-2}; H is the turbulent sensible - heat flux density, W m^{-2}, Q_m is the molecular thermal conductivity through the debris cover, W m^{-2}, Q_{act} is the energy change due to processes of water infiltration into the firn and the transfer of thermal conductivity deep into the active layer of the glacier, W m^{-2}

The model calculates snowmelt as long as snow is on the ground, then reverts to melt of ice under debris. It is supposed that there is snow on top of the debris, if the snow depth (H_{snow}) according to the input data is >=0, excluding cases when H_{snow} is thin (less than 2 cm), and the surface albedo is less than 0.5 according to measurements.

The A-Melt model is the only model in this intercomparison experiment that does not assume a constant ice temperature of 0ºC. The temperature in the surface ice layer can decrease below zero if the energy balance is negative, and warm back to 0ºC. The melting can occur only if the temperature of the surface ice layer has reached 0ºC.
The temperature of the ice surface layer is calculated as:

$$T_{\text{ice}}^{t} = T_{\text{ice}}^{t-1} + \frac{Q_m + Q_{\text{act}}}{c_{\text{ice}}\rho_{\text{ice}}\Delta h_{\text{ice}}}\Delta t, \text{ K} \quad \text{(S11)}$$

where T_{ice}^{t} is the temperature of the ice surface layer on this time step, T_{ice}^{t-1} is the temperature of the ice surface layer on the previous time step, Q_m is the molecular thermal conductivity through the debris cover, W m^{-2}, Q_{act} is the molecular thermal conductivity in the active layer, W m^{-2}, c_{ice} is the ice heat capacity, ρ_{ice} – ice density (set to 917 kg m^{-3}), Δh_{ice} – thickness of ice surface layer (set with the parameter ΔT_{prof}), Δt is the time step.
Q_{act} is calculated as:

$$Q_{act} = \lambda_{ice}\frac{T_{act} - T_{ice}}{h_{act}} \quad \text{(S12)}$$

where h_{act} is active layer thickness, m; T_{ice} is the temperature of the surface layer of ice, underlying debris; T_{act} is active layer bottom temperature, K, set as a constant value, λ_{ice} - the thermal conductivity of the ice, calculated according to ice density (Sturm et al., 1997), W m^{-1} K^{-1}.

The model uses a simplified bulk aerodynamic approach to calculate turbulent sensible and latent heat fluxes, using a formula developed by Kuzmin (1961) specifically for turbulent heat and moisture transfer over snow and ice surfaces. This approach uses constant bulk coefficients.

Maximum air humidity at the temperature of the ice surface, e_0, was calculated as the partial pressure of water vapor of the saturated air at the temperature:

$$Q_m = \lambda_m \frac{T_m - T_{ice}}{h_m} \quad \text{(S14)}$$

where T_m is debris surface temperature, T_{ice} is the temperature of the surface layer of ice, underlying debris. We assume the linear distribution of the air temperature in pores of debris, as the model has one layer of the debris.

The ice, covered with debris, is melting under the influence of the heat flux conducted through the debris by means of molecular thermal conductivity Q_m:

$$Q_m = \lambda_m \frac{T_m - T_{ice}}{h_m} \quad \text{(S14)}$$

where λ_m is the thermal conductivity of the debris cover, W m^{-1} K^{-1}; h_m is the debris cover thickness, m; T_{ice} is the temperature of the surface layer of ice, underlying debris; T_m is debris surface temperature, K, calculated according to its heat balance.

Table S10. Values of physical and empirical parameters used by the A-Melt model. Constant per site parameters: ice density = 917 kg m^{-3}, $\rho_{OldSnow} = 0.45$, $\Delta T_{prof} = 100$ cm, $\Delta T = 60$ min, $\alpha_{snow} = 0.5$. h_m = debris thickness (cm); dh_m = surface layer of debris (cm); $\rho_{OldSnow}$ = mean density of old snow (kg m^{-3}); ΔT_{prof} = layer thickness of temperature profile of snow (cm); T_{act} = glacier active layer bottom temperature (°C); h_{ActIce} = glacier active layer depth (cm); specific heat of debris (C_{deb}) – set according to lithology and literature (Robertson, E, 1988); ρ_{deb} = debris density based on lithology (source: https://pubs.usgs.gov/of/1988/0441/report.pdf); α_{snow} = snow albedo.

Parameter	ARO	CN	DJA	LIR	MIA	PIR	SDF	TAP	TAS
ε_{snow} (-)	0.98	0.98	0.98	0.98	0.98	0.98	0.98	0.98	0.98
h_m (cm)	6	10	61	30	22	18	11	80	30
dh_m (cm)	6	10	10	10	10	10	10	10	10
T_{act} (°C)	0	-8	0	0	0	-1	-1	-2	0
h_{ActIce} (cm)	10	2	10	10	10	10	10	10	10
C_{deb} (J kg^{-1} K^{-1})	900	800	800	500	800	800	800	800	900
ρ_{deb} (kg m^{-3})	2670	2700	2750	2700	2700	2200	2700	2700	2600

THRED

The thermal resistance based energy balance model for debris-covered glaciers (THRED) was developed for calculating runoff from Himalayan debris-covered glaciers, in which the spatial distribution of the thermal properties of the debris mantle is estimated from remotely sensed multi-temporal data (Fujita and Sakai, 2014).

This is the only energy balance model in this intercomparison experiment that is run at **daily** resolution. The model calculates the following fluxes at the debris surface:

$$G_d = \frac{T_s}{R_T} = (1-\alpha)R_s + R_L - \varepsilon\sigma(T_s + 273.15)^4 + H_s + H_L \quad \text{(S15)}$$

where G_d is the conductive heat through debris, T_S the surface temperature; R_T the thermal resistance; α the surface albedo, R_S the downward solar radiation, R_L the downward long-wave radiation, ε the emissivity of debris surface, σ the Stefan-Boltzmann constant; H_S the sensible heat, H_L the latent heat.

Thermal resistance, a proxy of debris thickness, is defined as the debris thickness divided by the thermal conductivity of the debris layer as:

$$R_T = \frac{h}{\lambda} \quad \text{(S16)}$$

where R_T, h, and λ are the thermal resistance (m^2 K W^{-1}), thickness of debris layer (m), and thermal conductivity of debris (W m^{-1} K^{-1}), respectively. In the original study, the thermal resistance was calculated from surface temperature and albedo, which

are obtained from satellite data, and reanalysis meteorological data by assuming a linear temperature profile within the debris layer as:

$$G_d = \frac{T_s - T_i}{R_T} \tag{S17}$$

where G_d, T_s, and T_i are the conductive heat flux through the debris layer (W m^{-2}), surface temperature (ºC), and temperature at the interface of debris and ice (assumed to be 0 ºC), respectively. In the experiment, thermal resistance is given as the boundary conditions (thickness and thermal conductivity). In the original study, satellite based albedo was used to calculate net shortwave radiation while the SWout is a given input variable in the experiment. Downward longwave radiation is also a given input variable though it was estimated from temperature, relative humidity and solar radiation in the original study.

The turbulent heat fluxes are calculated based on simplified bulk approaches following Fujita and Sakai (2014). A constant bulk coefficient for the turbulent flux on the debris surface (C_d, dimensionless) was used in the original study. For this experiment the model was modified to participate in the sensitivity experiment (see Section 2 in manuscript), and the bulk coefficient was calculated as:

$$C_d = \left[\frac{\kappa}{\ln\left(\frac{z_t}{z_0}\right)}\right]^2 \tag{S18}$$

where κ, z_t, and z_0 are von Karman's constant (0.4, dimensionless), measurement height (m), and surface roughness length (m), respectively.

Table S11. Values of physical and empirical parameters used by THRED model.

Parameter	Value
Density of ice (kg m^{-3})	880

2.2. Simplified energy balance model

MCC19

The simplified energy balance model (SEB) (MCC19, McCarthy, 2025), is a one-dimensional, simplified energy-balance model for ice melt below debris.

The model computes explicitly the shortwave radiation flux and the conductive heat flux at the atmosphere-debris interface. Other energy fluxes are included implicitly in the free parameter terms of the simplified debris-surface energy balance. When the debris is snow-covered, the model sets the surface temperature of the debris to 0ºC. Conductive heat fluxes are calculated at intervals within the debris. The model does not deal explicitly with moisture within the debris. At the debris-ice interface, only a conductive heat flux is calculated. The temperature of the ice was fixed at 0ºC.

The model solves heat conduction through a debris layer as such:

$$\rho_d c_d \frac{\partial T_d}{\partial t} = \frac{\partial}{\partial z}\left(k_d \frac{\partial T_d}{\partial z}\right) \tag{S19}$$

where ρ_d is debris density (assumed 1496 kg m^{-3}), c_d is debris specific heat capacity (assumed 948 J kg^{-1}), k_d is debris thermal conductivity, t is time, z is depth within the debris, and T_d is debris temperature.

The boundary condition at the debris surface is the simplified debris-surface energy balance:

$$S\downarrow(t) - S\uparrow(t) + c_1[T_a(t) - T_d(0,t)] + c_2 - k_d \frac{\partial T_d(0,t)}{\partial z} = 0 \tag{S20}$$

where $S\downarrow$ is incoming shortwave radiation, $S\uparrow$ is outgoing shortwave radiation, T_a is air temperature, and c_1 and c_2 are free parameters to be calibrated. This equation has a similar form to the simplified (debris-free) energy balance of Oerlemans (2001). Surface temperature is determined iteratively for each model timestep using Newton's method, following Reid and Brock (2010).

The boundary condition at the ice surface is the temperature of melting ice, T_i (273.15 K):

$$T_d(h,t) = T_i \quad \text{(S21)}$$

where h is debris thickness.

Melt rate, M, is computed as follows:

$$M(t) = \frac{\Delta t}{\rho_i L_f} k_d \frac{\partial T_d(h,t)}{\partial z} \quad \text{(S22)}$$

where Δt is the model timestep, ρ_i is ice density (assumed 915 kg m^{-3}), and L_f is the latent heat of fusion of water (334000 J kg^{-1}).

For this intercomparison experiment, the debris was discretised into 0.01 m thick layers (or ten thinner layers if debris thickness was < 0.1 m), following Reid and Brock (2010). All the layers were considered to have the same physical properties.

No spin-up period was used. A linear temperature gradient through the debris was used as the initial condition, again following Reid and Brock (2010), where debris surface temperature was the first recorded air temperature value of each time series and the ice surface temperature was the temperature of melting ice, as follows:

$$T_d(z,0) = [T_a(l) - T_i]z \quad \text{(S23)}$$

Additional input parameters include debris density (assumed 1496 kg m^{-3}) and debris specific heat capacity (assumed 948 J kg^{-1}). Two free parameters, c_1 and c_2 are determined by calibration for each site using the observed surface temperature and surface lowering data provided. This was done using a multiparameter multiobjective optimisation approach, following Rye et al. (2010):

$$f_{agg}(c_1,c_2) = [f_1^{norm}(c_1,c_2) + f_2^{norm}(c_1,c_2)] \quad \text{(S24)}$$

where f_{agg} is the aggregate objective function that was minimised, and f_1^{norm} and f_2^{norm} are the individual normalised objective functions f_{agg} is composed of.

The two individual objective functions $f_1(c_1, c_2)$ and $f_2(c_1, c_2)$ used in the optimisation procedure, prior to normalisation, were as follows:

$$f_1(c_1,c_2) = \frac{1}{n}\sum_{d=1}^{n}\left|\frac{m_{obs}^d - m_{mod}^d}{d-1}\right| \quad \text{(S25)}$$

$$f_2(c_1,c_2) = \frac{\sum_{t=1}^{n}(T_d^t(0)_{mod} - T_d^t(0)_{obs})^2}{\sum_{t=1}^{n}\left(T_d^t(0)_{obs} - \overline{T_d(0)_{obs}}\right)^2} \quad \text{(S26)}$$

where n is the number of observations, m_{mod}^d and m_{obs}^d are modelled and observed cumulative melt at day d, and $T_d^t(0)_{mod}$ and $T_d^t(0)_{obs}$ are the modelled and observed surface temperatures for timestep t. The first of these objective functions is the mean absolute error of cumulative melt per day. The second is 1-the Nash-Sutcliffe Efficiency coefficient of the surface temperature record. Both were normalised prior to minimisation according to:

$$f_n^{norm}(c_1,c_2) = \frac{f_n(c_1,c_2) - f_n^{min}}{f_n^{max} - f_n^{min}} \quad \text{(S27)}$$

where f_n^{min} and f_n^{max} are minimum and maximum expected objective function values. These were set to 0 and 0.0056 m i.e. d^{-1}, respectively, for the melt function, and to 0 and 0.5, respectively for the surface temperature function.

Table S12. Optimal free parameter values determined for the nine sites for model MCC19.

Site	c_1 (W m^{-2} K^{-1})	c_2 (W m^{-2})
Arolla	64.8	88.1
Changri-Nup	56.2	214
Djankuat	34.7	8.63
Lirung	54.6	96.6
Miage	45.8	-33.7
Piramide	48.0	-64.8
Suldenferner	40.2	78.3
Tapado	32.6	-24.0
Tasman	61.0	-34.3

Overview tables for EB and SEB

Table S13. Overview of the net shortwave radiation (S_{net}) calculation methods by each model.

Model	S_{net} Calculation
DEB_{CF}	Both $S_{\downarrow}$ and $S_{\uparrow}$ from observations
ROU15	Both $S_{\downarrow}$ and $S_{\uparrow}$ from observations
GRO17_{B}	Both $S_{\downarrow}$ and $S_{\uparrow}$ from observations
d2EB	Both $S_{\downarrow}$ and $S_{\uparrow}$ from observations
DEB_{PG}	Both $S_{\downarrow}$ and $S_{\uparrow}$ from observations
GRO17_{A}	Both $S_{\downarrow}$ and $S_{\uparrow}$ from observations
A-Melt	Both $S_{\downarrow}$ and $S_{\uparrow}$ from observations
THRED	Both $S_{\downarrow}$ and $S_{\uparrow}$ from observations
MCC19	Both $S_{\downarrow}$ and $S_{\uparrow}$ from observations

Table S14. Overview of the net longwave radiation (L_{net}) calculation methods by each model.

Model	L_{net} Calculation
DEB_{CF}	$L_{\downarrow}$ from measurement, $L_{\uparrow}$ calculated from internally computed T_s
ROU15	$L_{\downarrow}$ from measurement, $L_{\uparrow}$ calculated from internally computed T_s
$GRO17_{B}$	$L_{\downarrow}$ from measurement, $L_{\uparrow}$ calculated from internally computed T_s
d2EB	$L_{\downarrow}$ from measurement, $L_{\uparrow}$ calculated from internally computed T_s
DEB_{PG}	$L_{\downarrow}$ from measurement, $L_{\uparrow}$ calculated from internally computed T_s
$GRO17_{A}$	$L_{\downarrow}$ from measurement, $L_{\uparrow}$ calculated from internally computed T_s
A-Melt	$L_{\downarrow}$ from measurement, $L_{\uparrow}$ calculated from internally computed T_s
THRED	$L_{\downarrow}$ from measurement, $L_{\uparrow}$ calculated from internally computed T_s
MCC19	$L_{\downarrow}$ from measurement, $L_{\uparrow}$ calculated from internally computed T_s

Table S15. Overview of the sensible heat flux (SH) calculation methods by each model.

Model	SH Calculation
DEB_{CF}	Bulk aerodynamic method using Richardson number (Ri), as in Reid and Brock (2010). Stability functions calculated as a function of Ri.
ROU15	Simplified bulk approach (Nicholson and Benn, 2006). No stability corrections, assumption of neutral conditions.
$GRO17_{B}$	Following Evatt et al. (2015) with a non-linear wind-speed profile within the porous debris layer.
d2EB	Simplified bulk approach following Steiner et al. (2018). No stability corrections, assumption of neutral conditions.
DEB_{PG}	Bulk aerodynamic method using Richardson number (Ri), as in Reid and Brock (2010). Stability functions calculated as a function of Ri.
$GRO17_{A}$	Simplified approach as in Nicholson and Benn (2006). No stability corrections.
A-Melt	Simplified bulk approach, with constant coefficients (Kuzmin, 1961): $H = (\alpha_1 + \beta_1 u^2)(T_2 - T_0)$.
THRED	Simplified bulk approach following Fujita and Sakai (2014). No stability corrections, assumption of neutral conditions.
MCC19	Simplified bulk approach following Steiner et al. (2018). No stability corrections, assumption of neutral conditions.

Table S16. Overview of the latent heat flux (LE) calculation methods by each model.

Model	LE Calculation
DEB_{CF}	Same as for SH, as in Reid and Brock (2010). RH_s was assumed to be 100% (saturated surface) during rain.
ROU15	Simplified bulk approach (Nicholson and Benn, 2006). No stability corrections, assumption of neutral conditions. Debris is assumed saturated when it rains; otherwise, the flux is zero.
$GRO17_{B}$	Evaporative heat flux within the debris.
d2EB	Simplified bulk approach following Steiner et al. (2018). Debris surface moisture is calculated based on a parameterisation developed in Steiner et al. (2018).
DEB_{PG}	Same as for SH, as in Reid and Brock (2010). Calculated assuming that $RH_s = 100\%$ when air RH is 100%.
$GRO17_{A}$	No latent heat flux included.
A-Melt	Simplified bulk approach, with constant coefficients (Kuzmin, 1961): $LE = (\alpha_2 + \beta_2 u^2)(e_2 - e_0)$.
THRED	Simplified bulk approach following Fujita and Sakai (2014), including dependence on debris surface wetness. No stability corrections, assumption of neutral conditions.
MCC19	Simplified bulk approach following Steiner et al. (2018). No stability corrections, assumption of neutral conditions.

Table S17. Overview of the heat flux provided by liquid precipitation (P) calculation methods by each model.

Model	P Calculation
DEB_{CF}	Yes, as in Reid and Brock (2010).
ROU15	Yes, as in Reid and Brock (2010).
$GRO17_B$	No
d2EB	No
DEB_{PG}	No
$GRO17_A$	No
A-Melt	No
THRED	No
MCC19	No

Table S18. Overview of the ground heat flux (G) calculation methods by each model.

Model	G Calculation
DEB_{CF}	Fourier's law and iterative Newton-Raphson method to vary debris surface temperature and solve the energy balance, as in Reid and Brock (2010).
ROU15	Fourier's law and iterative Newton-Raphson method to vary debris surface temperature and solve the energy balance, as in Reid and Brock (2010).
$GRO17_B$	Fourier's law: simplified approach assuming a linear temperature gradient between T_s and T_i.
d2EB	Fourier's law and iterative Newton-Raphson method to vary debris surface temperature and solve the energy balance, as in Reid and Brock (2010).
DEB_{PG}	Fourier's law and iterative Newton-Raphson method to vary debris surface temperature and solve the energy balance.
$GRO17_A$	Fourier's law: simplified approach assuming a linear temperature gradient between T_s and T_i.
A-Melt	Simplified approach, one layer, linear temperature gradient between debris surface and ice surface.
THRED	Simplified approach, one layer, linear temperature gradient between debris surface and ice surface.
MCC19	No

Table S19. Overview of snow conditions and snowmelt calculation methods by each model.

Model	Snow Conditions and Snowmelt Calculation
DEB_{CF}	Yes. The model checks the snow depth record and calculates snowmelt as long as snow is on the ground, then reverts to the melt of ice under debris.
ROU15	When there is snow on the surface, the model assumes fluxes are zero except for the ground heat flux and the conductive heat flux at the snow/debris surface interface.
$GRO17_B$	No. Sub-debris ice melt was set to zero if the height of the snow cover was >0.0 m.
d2EB	No.
DEB_{PG}	No.
$GRO17_A$	No. Sub-debris ice melt was set to zero if the height of the snow cover was >0.0 m.
A-Melt	Yes. The model calculates snowmelt as long as snow is on the ground, then reverts to the melt of ice under debris. Snow on top of the debris is accounted for if snow depth (H_{snow}) is ≥ 0, except for thin snow layers (<2 cm) with surface albedo < 0.5.
THRED	Yes. Described in Fujita and Sakai (2014).
MCC19	No.

Table S20. Overview of debris properties required by each model. The parameters are as follows: h_d = debris thickness, k = thermal conductivity, z_0 = aerodynamic surface roughness length, ε = debris surface emissivity, c_d = debris specific heat capacity, ρ_d = debris density, ϕ = debris porosity, u^* = friction velocity, γ = wind speed attenuation constant, and Φ = fraction of debris embedded in ice.

Model	Parameters
DEB_{CF}	h_d, k, z_0, ε, c_d, ρ_d
ROU15	h_d, k, z_0, ε, c_d, ρ_d
$GRO17_B$	h_d, k, z_0, ε, u^* , γ, Φ
d2EB	h_d, k, z_0, ε, ϕ, ρ_d, c_d
DEB_{PG}	h_d, k, z_0, ε, c_d, ρ_d
$GRO17_A$	h_d, z_0, k, ε, Φ, u^*
A-Melt	h_d, k, ε, ϕ, c_d, ρ_d
THRED	h_d, k, z_0, ε
MCC19	h_d, k, c_d, ρ_d

2.3. Enhanced temperature index models

The KO2 model is an enhanced temperature index model and is considered in this category in this study. However in this Supplement the KO2 model is described after KM1 and KP1 in the temperature-index models section because it has several similarities with those.

$DETI_m$

The debris enhanced temperature index model (DETI) was developed by Carenzo et al. (2016) and includes a temperature factor (TF), a shortwave radiation factor (SRF), and a lag factor (lag) to account for the time it takes to transfer energy through the debris. Each of these three parameters needs to be calibrated as a function of debris thickness, as in equations 6, 7 and 8 in Carenzo et al. (2016).

A slight modification with respect to the original model has been implemented for this intercomparison experiment, and therefore we introduce the *m* subindex in the DETI acronym ($DETI_m$). Here, the term *i-lag*, accounting for the time lag of the energy transfer between the debris surface and the ice surface, is also applied to the temperature threshold condition. That is, melt is set to zero if the temperature was below T_T at the time step *i-lag*. Conversely, melt occurs if the temperature at the time step *i-lag* was above T_T (see Equation 1 below). This accounts for the delay in energy transfer through the debris layer also to the temperature threshold. For instance, if temperature drops to zero after a few hours of high temperatures, melt will only stop after the lag from the last time step with temperature above zero has reached the ice. Conversely, after a cold period, melt will not start immediately after temperature crosses T_T, but will start after that lag time has passed.

$$M = \begin{cases} TF \cdot T(i - lag_T) + SRF \cdot (1 - \alpha) \cdot I(i - lag_I) & T(i - lag) > T_T \\ 0 & T(i - lag) \leq T_T \end{cases} \quad \text{(S28)}$$

The DETI model is calibrated against hourly melt rate simulations from the DEB_{CF} model, as in the original paper by Carenzo et al. (2016) where the model was developed. For each site, the *lag*, *TF* and *SRF* parameters are parameterised as a function of debris thickness. Therefore, the DEB_{CF} runs for the debris thicknesses used in Experiment 3 of the model intercomparison (1, 2, 4, 6, 8, 10, 12, 15, 20, 30, 50, 100 cm) were used. For each thickness, a range of parameters was used to run the model and the highest Nash and Sutcliffe Efficiency between DETI and DEB_{CF} was sought to obtain the optimal parameters. With the optimal parameters for each thickness, equations 2, 3 and 4 are derived, and the parameters lag_1, lag_2, TF_1, TF_2, SRF_1 and SRF_2 obtained from them. We assumed that the optimal curve fitting functions are the same as those in Carenzo et al. (2016), i.e. linear for the lag parameter, power law for TF and exponential for SRF. The optimal parameters obtained are in Table S21.

$$lag = lag_T = lag_I = lag_1 \cdot d + lag_2 \quad \text{(S29)}$$

$$TF = TF_1 \cdot d^{TF_2} \quad \text{(S30)}$$

$$SRF = SRF_1 \cdot e^{SRF_2 \cdot d} \quad \text{(S31)}$$

Table S21. $DETI_m$ calibrated and uncalibrated model parameters.

Site	lag_1	lag_2	TF_1	TF_2	SRF_1	SRF_2
AROLLA	21.93	-1.23	0.019	-0.526	0.0081	-13.8533
CHANGRI NUP	24.56	-1.45	0.017	-0.780	0.0039	-13.9848
DJANKUAT	10.99	-0.55	0.044	-0.212	0.0095	-6.1140
LIRUNG	15.34	-0.67	0.069	-0.127	0.0114	-10.3353
MIAGE	19.97	-1.00	0.021	-0.441	0.0093	-13.1247
PIRAMIDE	19.97	-1.00	0.011	-0.611	0.0073	-13.5738
SULDENFERNER	25.44	-1.05	0.017	-0.368	0.0083	-13.8533
TAPADO	21.93	-1.23	0.015	-0.667	0.0061	-12.0041
TASMAN	12.98	-0.65	0.032	-0.475	0.0095	-8.8402
Uncalibrated (Carenzo et al. 2016)	21.54	-1.19	0.016	-0.621	0.0079	-11.2100

2.4. Temperature index models

KM1 and KP1

These are temperature-index models configured as in Winter-Billington et al. (2020). The two models share the same model structure with the same fixed-effects parameters, but different random-effects parameters. The models were fitted using data from 27 debris-covered glaciers around the world (Winter-Billington et al., 2020). They estimate the underlying relation between melt, air temperature, and debris thickness (fixed effects) while accounting for the statistical variation of melt factors among glaciers and among glacier-years (random effects). Total ice melt over a period of time is predicted in these models as the product of modelled melt factors and daily mean positive degree days. The main model equations are as follows:

$$\mathrm{PDD} = \delta d \sum_{i=1}^{n_d} (T_i - T_b)\,\delta(T_i) \qquad \text{with} \qquad \delta(T_i) = \begin{cases} 1, & \text{if } T_i \geq T_b, \\ 0, & \text{if } T_i < T_b. \end{cases} \quad \text{(S32)}$$

where subscript i is one day in the observation period of n_d days, T_i is mean air temperature on day i, T_b is a threshold air temperature below which ablation ceases and $\delta(T_i)$ is a binary variable that sets ablation on day i to zero when $T_i \leq T_b$, and

$$melt = k \times D_i \quad \text{(S33)}$$

where k is a predicted melt factor (mm day^{-1} °C^{-1}) and D_i is daily mean PDD (PDD/n_d).

The value of k is the melt factor (mm day^{-1} C^{-1}) dependent **on debris thickness** (h) and fitted parameters according to equation:

$$k = 10^{(b_0 + b_{0i} + b_{0ij}) + (b_1 + b_{1i} + b_{1ij}) \times h} \quad \text{(S34)}$$

where g is glacier identity and y is the nested glacier-year. The difference between KM1 and KP1 is the data used in model fitting, which resulted in different fitted coefficient values (see Winter-Billington et al. (2020) for details). The fixed- effects coefficients for models KM1 and KP1 are in Table S22. The random-effects coefficients for models KM1 and KP1 are in Tables S23 to S26 (see Winter-Billington et al. (2020) for more details).

The only model component that is calibrated is T_b for the calculation of Di as input to model KM1. For the calibrated runs (model KM1), the fitted values of T_b are shown in Table S22. For uncalibrated runs (model KP1), $T_b = 0$.

With the time series of Ti that were provided for each site, time series of Di were calculated using T_b = [-10, 9]. The model was run using every set of Di. The value of T_b that resulted in the smallest RMSE between cumulative observed and predicted melt was selected (Table S22). The model parameters were fitted assuming $T_b = 0$, so the calibrated values of T_b are not physically meaningful.

Table S22. Summary of fixed-effects coefficients per site, for models KM1 and KP1, as well as the calibrated values of T_b for each site for KM1.

Site	KM1			KP1	
	b_0	b_1	T_b	b_0	b_1
AROLLA	0.4937	-1.4460	-2	0.6215	-1.4572
CHANGRI NUP	0.2691	-1.4614	-8	0.6215	-1.4572
DJANKUAT	0.5981	-1.4179	0	0.6215	-1.4572
LIRUNG	0.5583	-1.4179	-1	0.6259	-1.4034
MIAGE	0.4422	-1.4461	-3	0.6223	-1.4505
PIRAMIDE	0.5479	-1.4405	-1	0.6215	-1.4572
SULDENFERNER	0.4465	-1.4506	-3	0.6215	-1.4572
TAPADO	0.5981	-1.4179	0	0.6215	-1.4572
TASMAN	0.2150	-1.4630	-10	0.6215	-1.4572

Table S23. Random effects coefficients for model KM1. Glacier-specific coefficients.

Glacier	β_0	β_1
Baltoro glacier	0.0357340606696045	-0.183784796122387
Barpu Glacier	0.0142430361478071	-0.0732537392184386
Batal glacier	-0.1139397559226	0.586006601426085
Chorabari Glacier	-0.0936873740159294	0.481846023280708
Dokriani Glacier	-0.159065988224529	0.818096543753797
Eliot Glacier	0.260196953533077	-1.33822591232525
Franz Josef Glacier	0.000503675392434745	-0.00259046652936516
Ghiacciaio del Belvedere	0.0559567421848158	-0.287792610949187
Hailuogou Glacier	0.0804089622140197	-0.413553477827503
Koxkar Glacier	-0.147602975966774	0.759140816554963
Larsbreen	0.0316679375651566	-0.162872218535068
Lirung Glacier	0.0340603702227083	-0.175176819106456
Miage Glacier	0.0048722633088835	-0.0250586613974906
Qingbingtan Glacier No. 72	-0.0567097700710563	0.291665539382937
Rakhiot Glacier	0.0591447276272265	-0.304188830014309
Southern Inylchek Glacier	0.0452024202172116	-0.232481775248828
Venerocolo Glacier	-0.0464798277217959	0.239051640743079
Vernagtferner	-0.00450545716029045	0.0231721421328688

Table S24. Random effects coefficients for model KM1. Glacier-year-specific coefficients.

Glacier:year	β_0	β_1
Baltoro glacier:2004	0.121258503701998	0.122278149313058
Barpu Glacier:1987	0.0156266115392138	0.0157580135059646
Batal glacier:2014	-0.0759629069769631	-0.0766016683201904
Chorabari Glacier:2003-2010	-0.300552483575998	-0.303079786910736
Chorabari Glacier:2010	0.0298298993709972	0.0300807347767082
Dokriani Glacier:2010	0.0241620317599601	0.0243652068683952
Dokriani Glacier:2011	-0.0240436636760613	-0.0242458434440167
Dokriani Glacier:2012	-0.00353733119957876	-0.00356707611743936
Dokriani Glacier:2013	0.104982877014882	0.105865663182587
Eliot Glacier:1987- 1989	-0.0377894787305967	-0.0381072451136174
Franz Josef Glacier:2012	-0.00259775140087978	-0.0026195955250745
Ghiacciaio del Belvedere:2002	0.108843577109364	0.10975882735824
Hailuogou Glacier:2009	0.106738217036862	0.107635763610597
Koxkar Glacier:2004	0.0613835685357198	0.0618997342835874
Larsbreen:2003	-0.0340250041984198	-0.0343111156474153
Lirung Glacier:1995	0.0243306475161885	0.0245352404906747
Lirung Glacier:2013	0.0551957186630032	0.0556598516562845
Lirung Glacier:2014	-0.396290376691568	-0.399622726431689
Miage Glacier:2005	0.0535715883768126	0.0540220642881777
Miage Glacier:2010	0.0324151758431857	0.03268775047318
Miage Glacier:2011	0.0244809107344371	0.0246867672510775
Qingbingtan Glacier No. 72:2008	0.0758207738285469	0.0764583399942274
Rakhiot Glacier:1986	0.00615363159401982	0.00620537661193907
Southern Inylchek Glacier:2005	0.0177847873556592	0.0179343371176734
Venerocolo Glacier:2007	-0.0737453147321626	-0.0743654286557821
Vernagtferner:2010	0.0859657912014107	0.0866886653836225

Table S25. Random effects coefficients for model KP1. Glacier-specific coefficients.

Glacier	β_0	β_1
24k glacier	-0.0513122597179868	0.238585166994192
Baltoro glacier	-0.000598337394081189	0.00278207250801877
Barpu Glacier	-0.00662116445614081	0.0307862416534858
Batal glacier	-0.0810552911548811	0.376880501506569
Chorabari Glacier	-0.141233390473522	0.656688912873378
Djankuat Glacier	0.00892381079289292	-0.0414927913903704
Dokriani Glacier	-0.167670640338444	0.779613448034292
Eliot Glacier	0.271686662329542	-1.26325381221257
Franz Josef Glacier	-0.0130934137054091	0.0608800764690168
Ghiacciaio del Belvedere	0.0464673851539856	-0.216058090360439
Hailuogou Glacier	0.0339672459261235	-0.157936545499207
Ice-cored Fox Glacier Moraine	0.0579433215891738	-0.269417428379309
Khumbu Glacier	0.0747926300215065	-0.34776118264308
Koxkar Glacier	-0.127554834824709	0.593088118411241
Larsbreen	0.0298702576801357	-0.138886894787769
Lirung Glacier	0.0165455990074614	-0.0769316051156168
Maliy Aktru	0.0352657909355486	-0.163974353610288
Miage Glacier	0.00935199836185992	-0.0434837230548166
Qingbingtan Glacier No. 72	-0.03405061833338	0.158324199830108
Rakhiot Glacier	0.0281443510389046	-0.130861995348968
Southern Inylchek Glacier	0.0804509502631034	-0.37407051470461
Summit Crater Glacier	0.0457376248258707	-0.212664944342198
Svínafellsjökull	-0.0513805148502741	0.238902530957979
Venerocolo Glacier	-0.0305396433717916	0.141999318561444
Vernagtferner	-0.0142434356348657	0.0662273010035504
Zopkhito Glacier	-0.0197940836708316	0.0920359926469375

Table S26. Random effects coefficients for model KP1. Glacier-year-specific coefficients.

Glacier:Year	β_0	β_1
24k glacier:2008	0.0240883566892971	0.0582565436236891
Baltoro glacier:2004	0.0159771345852822	0.0386399392019384
Barpu Glacier:1987	-0.0427784001953234	-0.103457523868276
Batal glacier:2014	0.0553787493979968	0.13393086841674
Chorabari Glacier:2003-2010	-0.234272539312624	-0.566576980834992
Chorabari Glacier:2010	0.0179004850394911	0.0432914706901386
Djankuat Glacier:2007	0.00589414175292368	0.0142547011646491
Dokriani Glacier:2010	0.0216836054138076	0.0524407671723665
Dokriani Glacier:2011	-0.0106504367408129	-0.0257575741095776
Dokriani Glacier:2012	0.0114889875766503	0.0277855693762846
Dokriani Glacier:2013	0.095923494245830 6	0.231986403188386
Eliot Glacier:1987- 1989	-0.0207367232494906	-0.050150777746208
Franz Josef Glacier:2012	-0.060636420035475	-0.146646294495902
Ghiacciaio del Belvedere:2002	0.0528924858250661	0.127917958355475
Hailuogou Glacier:2009	0.015525174784138	0.0375468959441054
Ice-cored Fox Glacier Moraine:2007	-0.00624997167821862	-0.0151152588952132
Khumbu Glacier:1999	0.327258636495271	0.791459429097824
Koxkar Glacier:2004	0.254123631601645	0.614585902274912
Koxkar Glacier:2010	-0.161925960996869	-0.391610226147693
Larsbreen:2003	0.019435035098718	0.0470027069368109
Lirung Glacier:1995	0.0849223550501107	0.20538067189122
Lirung Glacier:2013	0.0391842662233663	0.0947652820010778
Lirung Glacier:2014	-0.344971135240858	-0.834296263887609
Maliy Aktru:2007	-0.17752924922947	-0.429346035747331
Miage Glacier:2005	0.0264769316595675	0.0640331984511162
Miage Glacier:2010	-0.0431587960706609	-0.104377493179246
Miage Glacier:2011	-0.0228850941217367	-0.0553465104005023
Qingbingtan Glacier No. 72:2008	0.11709403870841	0.283186356880931
Rakhiot Glacier:1986	-0.0965425089034547	-0.233483460661867
Southern Inylchek Glacier:2005	-0.024007803110899	-0.0580617286301002
Summit Crater Glacier:2008	0.196198999245799	0.474497937153413
Svínafellsjökull:2013	-0.148115619288772	-0.358210572341782
Venerocolo Glacier:2007	-0.0581675440027374	-0.140675435372641
Vernagtferner:2010	0.0717589733940422	0.173545660164465
Zopkhito Glacier:2009	-0.000577280610070789	-0.0013961256667476

KO2 (ETI)

This model is configured as KM1/KP1 with a modified calculation of the melt factor k, now dependent on both debris thickness (h) and **mean net shortwave radiation** (SW_{net}):

$$k = 10^{b_0 + b_1 \times h + b_2 \times SW_{net}} \quad \text{(S35)}$$

In Winter-Billington et al. (2020), the models were fit using the data that were also used in this intercomparison project, from Lirung Glacier and Miage Glacier. Therefore, the models were refit using the data in Winter-Billington et al. (2020) with the data from Lirung and Miage Glaciers excluded. The refitted fixed-effect coefficient values for KO2 are in Table S27, and random effects coefficients in Table S28.

Table S27. Summary of fixed-effects coefficients for the KO2 model.

Parameter	b_0	b_1	b_2
All sites	-0.6783	-1.4442	0.0058

Table S28. Random-effects coefficients for model KO2. Glacier (top) and glacier-year (bottom) specific coefficients.

Glacier	β_0	β_1
24k glacier	0.00407425627772242	-0.00028907189192505
Baltoro glacier	-0.0986121343590905	0.00699661519261567
Djankuat Glacier	-0.0124186768013377	0.000881115701927656
Franz Josef Glacier	0.0806347709649952	-0.00572110585442618
Ice-cored Fox Glacier Moraine	-0.144299356452944	0.010238162505367
Khumbu Glacier	0.302254699982923	-0.0214452290458508
Koxkar Glacier	-0.189638418599908	0.0134550077939038
Maliy Aktru	-0.159261366675735	0.0112997299167774
Southern Inylchek Glacier	0.0276884323677957	-0.00196451798498316
Summit Crater Glacier	0.0465263205303233	-0.00330108218456408
Svínafellsjökull	0.0884292163233635	-0.00627412841763036
Zopkhito Glacier	0.0546222564419513	-0.003875495731216
Glacier:Year	β_0	β_1
24k glacier:2008	$1.74986897826604 \times 10^{-6}$	$1.30962443856709 \times 10^{-7}$
Baltoro glacier:2004	$-4.50859186903996 \times 10^{-5}$	$3.37428811445672 \times 10^{-6}$
Djankuat Glacier:2007	$-5.63357348437098 \times 10^{-6}$	$4.21623881743798 \times 10^{-7}$
Franz Josef Glacier:2012	$3.67970669243553 \times 10^{-5}$	$-2.75393979265104 \times 10^{-6}$
Ice-cored Fox Glacier Moraine:2007	$-6.57671733778732 \times 10^{-5}$	$4.92209980180854 \times 10^{-6}$
Khumbu Glacier:1999	$1.3790846587808 \times 10^{-4}$	$-1.03212468729056 \times 10^{-5}$
Koxkar Glacier:2010	$-8.66353455218419 \times 10^{-5}$	$6.48390063189397 \times 10^{-6}$
Maliy Aktru:2007	$-7.26105408702559 \times 10^{-5}$	$5.43426622234825 \times 10^{-6}$
Southern Inylchek Glacier:2005	$1.27372621257994 \times 10^{-5}$	$-9.53273071730848 \times 10^{-7}$
Summit Crater Glacier:2008	$2.12535979209276 \times 10^{-5}$	$-1.59064659071256 \times 10^{-6}$
Svínafellsjökull:2013	$4.03685491116543 \times 10^{-5}$	$-3.02123411082499 \times 10^{-6}$
Zopkhito Glacier:2009	$2.49177410056761 \times 10^{-5}$	$-1.86487576957076 \times 10^{-6}$

Hyper-fit

The Hyper-fit model is a temperature-index melt model, developed by Anderson and Anderson (2016). The model takes a bare-ice melt rate and decreases that melt rate due to the insulating effects of debris cover. The shape of the debris thickness-melt relationship output by the model is hyperbolic and the rate of decline of that curve is defined by a characteristic debris thickness scale h_*.

In the model, the bare-ice melt rate $\dot{b}_{ice}$ is estimated using a degree-day factor for bare-ice DDF_{ice}:

$$\dot{b}_{ice} = DDF_{ice} \times T^{+} \tag{S36}$$

where and T^{+} is the positive degree-days defined as the mean hourly air temperature at 2m above the surface (when above 0° C) . Despite using an hourly time step the degree day nomenclature is still used as is convention (e.g., Hock, 2003).

At each hourly time step, the bare ice melt rate is then reduced based on:

$$\dot{b}_{debris} = \dot{b}_{ice} \left(\frac{h_*}{h_* + h_{debris}} \right) \tag{S37}$$

where $\dot{b}_{debris}$ is the sub-debris melt rate, h_{debris} is the local debris thickness, and h_* is the characteristic debris thickness scale. If ice is assumed to be at the freezing point, h_* can be estimated from physical inputs and parameters following:

$$h_* = \frac{kR}{(1-\phi)} \tag{S38}$$

where k and φ are the thermal conductivity and porosity of the debris cover and R is the thermal resistance of the debris layer. Here we define R as:

$$R = \frac{T_s^{-}}{L \rho_{ice} \dot{b}_{ice}} \tag{S39}$$

where L and ρ_{ice} the latent heat of fusion and density of ice, $\bar{T_s}$ the average debris surface temperature over the period used to estimate h_* and $\dot{b}_{ice}$ is the bare-ice melt rate over the period used to estimate h_*. We consider the case in which this model has two parameters: DDF_{ice} and h_*.

This model assumes that heat is transferred through debris by conduction. Sub-debris melt should therefore vary inversely with debris thickness (excluding the possibility for melt enhancement for debris less than ~ 3 cm). In other words the debris thickness-melt relationship (or Østrem's curve) for a given site should be hyperbolic as conduction is governed by the temperature gradient within the debris (e.g., Nicholson & Benn, 2006). In this formulation, sub-debris melt rates approach bare-ice melt rates as debris thins ($h_{debris} << h_*$) and asymptotes toward zero melt as debris thickens ($h_{debris} >> h_*$).

There are two input variables needed for this model: 1) 2 m air temperature, which can be from on glacier or off glacier sources; and 2) local debris thickness. If desired the model can also use thermal conductivity, thermal resistivity, and debris porosity as inputs, but in practice estimating h_* from empirical data appears to be effective. The model has two parameters, the bare-ice degree-day factor DDF_{ice} and the characteristic debris thickness h_*.

Uncalibrated (estimated) parameters

For uncalibrated simulations, values for the two parameters were derived from previous publications, independent from the data provided in this intercomparison project and therefore regarded as estimated instead of uncalibrated.

h_* values can be estimated if debris thickness-melt data (or Østrem's curves) are available. With debris thickness-melt data from each site, independent from the data provided in this intercomparison project, the modeller optimised both h_* and $\dot{b}_{ice}$ to obtain a best fit curve using Scipy's curve_fit package (see Table S24). If no Østrem curve was available the global mean value of 0.066 m was applied (Anderson and Anderson, 2016). In the case of the SDF site debris thickness-melt data were available but the data was too noisy to produce a viable estimate of h_*. For SDF debris less than 3 cm thick melt values ranged between 8.7 and 2.2 cm/day. The noise precluded the estimate of a unique, viable h_* value. For TAS debris thickness-melt values were available but varied between 10 m/yr and 0.5 m/yr between 18 and 28 cm debris thickness, so the global mean h_* value of 0.066 m was applied.

For the uncalibrated (estimated) h_* values the mean was 0.085±0.034 m (1σ) and ranged between 0.055 to 0.16 m. These numbers are similar to those presented in the global compilation of h_* values from Anderson and Anderson (2016) the h_* mean was 0.066±0.029 m (1σ) and ranged between 0.03 and 0.13 m.

The DDF_{ice} parameters applied at each site were derived from previous publications from each site, with two exceptions. In the case of PIR, a DDF_{ice} was applied from adjacent glaciers 2-5 km away (Bello and Yeso Glaciers; Table 1). In the case of CN, a DDF_{ice} was applied from Khumbu Glacier, 5 km away (Table 1). If DDF_{ice} values were provided in a publication those values were used. Otherwise the values of DDF_{ice} were calculated by the modeller using melt and air temperature data provided in each publication. For the uncalibrated DDF_{ice} parameters the mean was 0.45±0.27 mm/hr/K (1σ) and ranged between 0.023 to 1.1 mm/hr/K.

Calibrated parameters

Of the two hyper-fit model parameters one was calibrated. The characteristic debris thickness h_* was calibrated with the cumulative melt for each hour within the full measurement period at each site. The root mean squared error was then minimised for viable parameter choices. For sites that do not provide mean hourly melt rates (i.e., melt was measured using ablation stakes) the cumulative melt was interpolated to each hour using the mean melt rate provided by the ablation stakes. For the h_* values calibrated here the mean was 0.066±0.013 m (1σ) and ranged between 0.049 and 0.089 m. This excludes the two outliers, likely caused by low DDF_{ice} values from the literature (Table 1). These numbers are similar to those presented in the global compilation from Anderson and Anderson (2016) the h_* mean was 0.066±0.029 m (1σ) and ranged between 0.03 and 0.13 m.

The second parameter, the DDF_{ice} was not calibrated during the simulations in which h_* was calibrated. Instead at each site a value from the literature was applied (see below). The DDF_{ice} in principle could have been calibrated with the data provided for each site but no calibration was performed here.

Table S24. Hyper-fit literature (lit.) and calibrated (cal.) parameter values for each site.

Glacier	DDF_{ice} [mm hr^{-1} K^{-1}]	Reference for DDF_{ice}	h* (lit.) [m]	Reference for h* (lit.)	h* (cal.) [m]
ARO	0.5^{+}	Pellicciotti et al., 2005	0.075^{i}	Reid et al., 2012	0.056
CN	0.7^{+}	Kayastha et al., 2000	0.078^{i}	Lejeune et al., 2013	$>0.5^{\#}$
DJA	0.31^{+}	Lambrecht et al., 2011	0.16^{+}	Bozhinskiy et al., 1986	$0.45^{\#\#}$
LIR	0.33^{+}	Chand and Kayastha, 2018	0.068^{i}	Chand and Kayastha, 2018	0.066
MIA	$0.23^{\dagger}$	Brock et al., 2010	0.13^{i}	Brock et al., 2010	0.089
PIR	$0.3^{\dagger,\circ}$	Ayala et al., 2017	0.055^{i}	Ayala et al., 2016	0.049
SDF	0.36^{+}	M. McCarthy, personal comm.	$0.066^{\star}$	Global mean	0.06
TAP	$1.1^{\dagger}$	Ayala et al., 2017	$0.066^{\star}$	Global mean	0.061
TAS	$0.25^{\dagger}$	Kirkbride, 1995	$0.066^{\star}$	Global mean	0.083

$^{+}$ Reported value from literature or personal communication. † Calculated based on available bare-ice melt and air temperature data from cited paper. ^{i} Based on available debris thickness-melt data from cited paper. $^{\circ}$ For the PIR case, a DDF_{ice} was applied from Bello and Yeso Glaciers 2-5 km to the northwest. * No debris thickness-melt data was available from the literature so the global mean based on Anderson and Anderson (2016) was applied. For SDF and TAS debris-thickness-melt data were available but the data was too noisy to produce a viable h* value. $^{\#}$ The calibrated h* for CN never reaches a viable minimum for the CN case. Ultimately, a higher DDF_{ice} value would reduce the calibrated h* into a reasonable range. The model appears to be especially sensitive to input parameters for sites with low air temperatures but with high relative shortwave radiation input, as should be the case for all temperature index models solely dependent on air temperature. Note that in simulations for CN a calibrated value of 50 cm is used for h*, while a larger value could be used, the results do not change much even with a 200 cm value. $^{\#\#}$ The calibrated h* for DJA is a strong outlier amongst the population of calibrated h* values and the global compilation of h* values. Note that from the literature on DJA, Lambrecht et al. (2011) mentions a value for h* of 10 cm, their debris thickness-melt data produce an h* of 8.4 cm, but a back of the envelope calculation based on provided debris properties produces a much higher h* value. Using equation 3 with $k = 2.8$ W/m/K, $R = 10.2$ K m^2/W (the mean reported value from Lambrecht et al. (2011) for DJA), and $\phi = 0.42$, then $h* = 49$ cm. For extreme values of R from DJA, $h*$ can range from 34 to 75 cm. The modeler chose the reported value of 16 cm from Bozhinskiy et al. (1986). Ultimately, a higher DDF_{ice} value would reduce the calibrated h* into a viable range. This may also point to where the hyper-fit model assumptions break down.

DDF_{debris}

The simplest form of temperature index model with a single parameter is applied. Sub-debris melt b_{debris} is calculated using a degree-day factor DDF_{debris}:

$$\sum_{i=1}^{n} b_{debris} = DDF_{debris} \times \sum_{i=1}^{n} T^{+} \Delta t \tag{S40}$$

where and T^{+} is the positive degree-days defined as the mean hourly air temperature at 2 m above the surface (when above 0° C) and Δt is one hour. Despite using an hourly timestep the degree day nomenclature is still used as is convention (e.g., Hock, 2003).

The model accounts for the effect of debris by reducing (or increasing) the degree-day factor for bare ice to represent the melt suppressing (enhancing) effects of debris. As debris thickness is not used by the model, this model is not run in uncalibrated form, as this would not make sense.

The sub-debris degree-day factor was calibrated with the cumulative melt for each hour within the full measurement period at each site. The root mean squared error was then minimized to find the best-fit sub-debris degree-day factor. For sites that do not provide mean hourly melt rates (i.e., melt was measured at periods longer than 1 hour from ablation stakes) the cumulative melt was interpolated to each hour using the mean melt rate provided from the ablation stake measurements.

Table S25. Calibrated DDF_{debris} parameter values for each site.

Glacier	DDF_{debris} [mm hr^{-1} $°C^{-1}$]	RMSE [cm]
ARO	0.24	11
CN	0.69	16
DJA	0.13	3.8
LIR	0.06	3.8
MIA	0.066	5.3
PIR	0.064	6.4
SDF	0.125	2.1
TAP	0.078	3
TAS	0.055	1.4

Table S26. Model execution time for one single standard run over Miage, excluding the time to load and export the data, and programming language in which the model is written.

Model Execution time	Execution time (s)	Processor used	Model code language
$GRO17_A$	0.05	i7 processor	R
$GRO17_A$	0.05	i7 processor	R
DEB_{CF}	~1.8	i5 processor	Matlab
ROU15	~2	i7 processor	Python
A-Melt	~0.1	i5 processor	Fortran 90
THRED	~1	Xeon Bronze	Fortran 90
d2EB	~20	i7 processor	R
DEB_{PG}	~4	i5 processor	Matlab
MCC19	~4	i7 processor	Matlab
$DETI_m$	~0.001	i7 processor	Matlab
KM1/KP1	~0.003	DDR3	R
KO2	~0.001	DDR3	R
Hyper-fit	~0.00003	i7 processor	Python
DDF_{debris}	~0.000008	i7 processor	Python

3. Results

3.1. Performance of model ensemble at sites

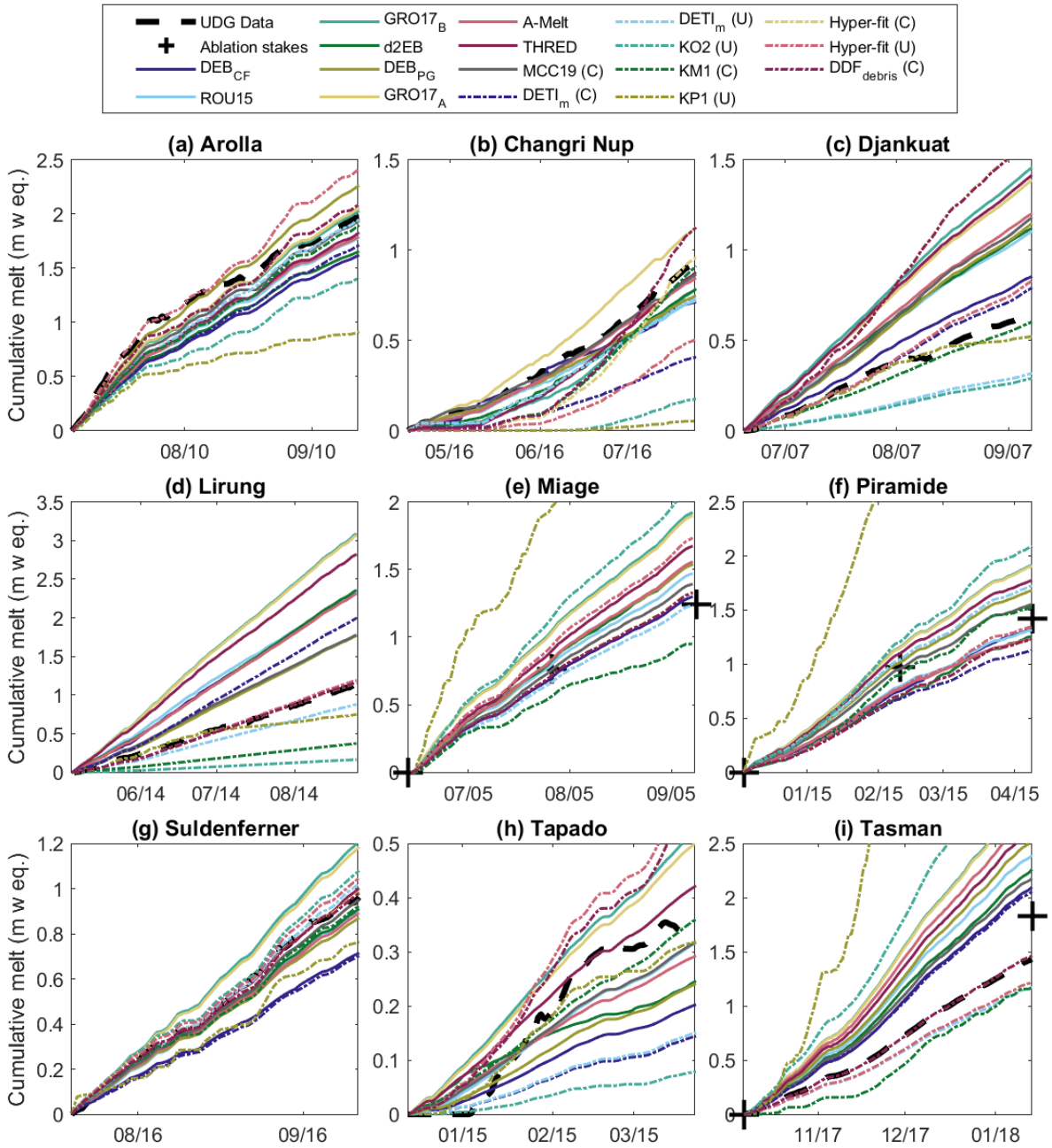

Figure S2. Comparison of cumulative melt simulations across all models with observed melt data at each site.

Table S27. Root mean square error (°C) of modelled surface temperature of debris across models and across sites at the hourly (h) and daily (d) scale. The last two columns correspond to the median and interquartile range (IQR) across sites per model, and the last row corresponds to the median across models per site.

Model	Resolution	ARO	CNU	DJA	LIR	MIA	PIR	SDF	TAP	TAS	Median (%)	IQR (%)
DEB_{CF}	h	2.3	2.8	4.8	7.7	2.5	4.5	2.7	3.0	3.3	3.0	1.9
DEB_{CF}	d	1.4	1.1	2.8	5.9	1.5	3.2	1.3	1.1	3.1	1.5	1.9
ROU15	h	3.0	3.8	3.9	6.8	3.8	4.5	5.5	5.1	2.9	3.9	1.6
ROU15	d	2.0	2.1	2.1	5.7	2.9	2.7	3.4	3.3	1.5	2.7	1.3
$GRO17_B$	h	3.7	5.6	7.6	15.6	6.6	5.9	8.4	11.2	7.1	7.1	3.2
$GRO17_B$	d	2.2	3.1	2.1	6.5	2.8	1.1	4.2	3.8	1.4	2.8	2.0
d2EB	h	2.9	4.6	4.8	7.0	5.6	6.8	5.5	9.7	4.4	5.5	2.3
d2EB	d	1.7	3.1	3.2	5.7	4.2	4.7	3.6	6.1	2.6	3.6	1.9
DEB_{PG}	h	1.5	2.6	3.3	2.0	2.0	3.6	3.3	2.8	3.2	2.8	1.3
DEB_{PG}	d	0.7	0.9	1.5	2.0	1.1	2.5	0.9	0.8	2.8	1.1	1.3
$GRO17_A$	h	3.8	5.9	8.4	15.9	7.0	6.1	8.6	12.1	7.2	7.2	3.5
$GRO17_A$	d	2.2	3.2	2.3	7.1	3.0	1.0	4.3	4.3	1.4	3.0	2.3
A-Melt	h	3.3	5.3	5.3	7.2	4.6	4.1	4.0	4.9	4.4	4.6	1.2
A-Melt	d	2.1	4.2	3.0	5.3	3.7	3.2	3.3	2.3	2.5	3.2	1.4
THRED	h	-	-	-	-	-	-	-	-	-	-	-
THRED	d	2.3	4.0	4.6	8.4	4.7	1.2	4.7	6.6	1.3	4.6	3.1
MCC19	h	3.2	4.4	3.4	2.0	2.7	2.8	4.2	3.7	2.7	3.2	1.1
MCC19	d	3.0	3.8	2.1	2.4	2.3	0.8	4.0	3.4	2.4	2.4	1.2
Median (%)	h	3.1	4.5	4.8	7.1	4.2	4.5	4.9	5.0	3.8	Overall	4.5
Median (%)	d	2.1	3.1	2.3	5.7	2.9	2.5	3.6	3.4	2.4	Overall	2.8

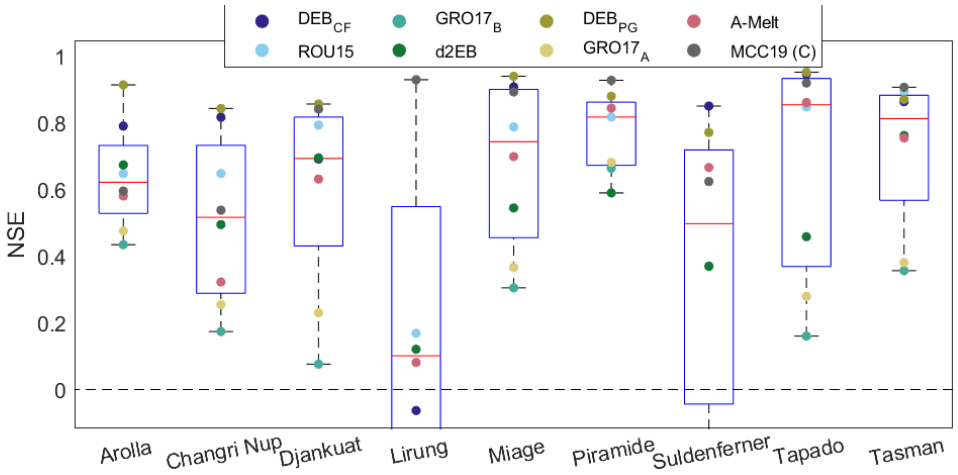

Figure S3. Validation of the energy balance model simulations against surface temperature across sites. Statistical boxes for each site show the distribution of the Nash Sutcliffe Efficiency of surface temperature for each model. Note that the THRED model is run at daily resolution and therefore not validated with NSE as discussed in the text. $GRO17_A$ and $GRO17_B$ are negative at Lirung (-4.1 and -3.4, respectively) and Suldenferner (-0.55 and -0.46, respectively) but are not displayed for better visibility of the plot.

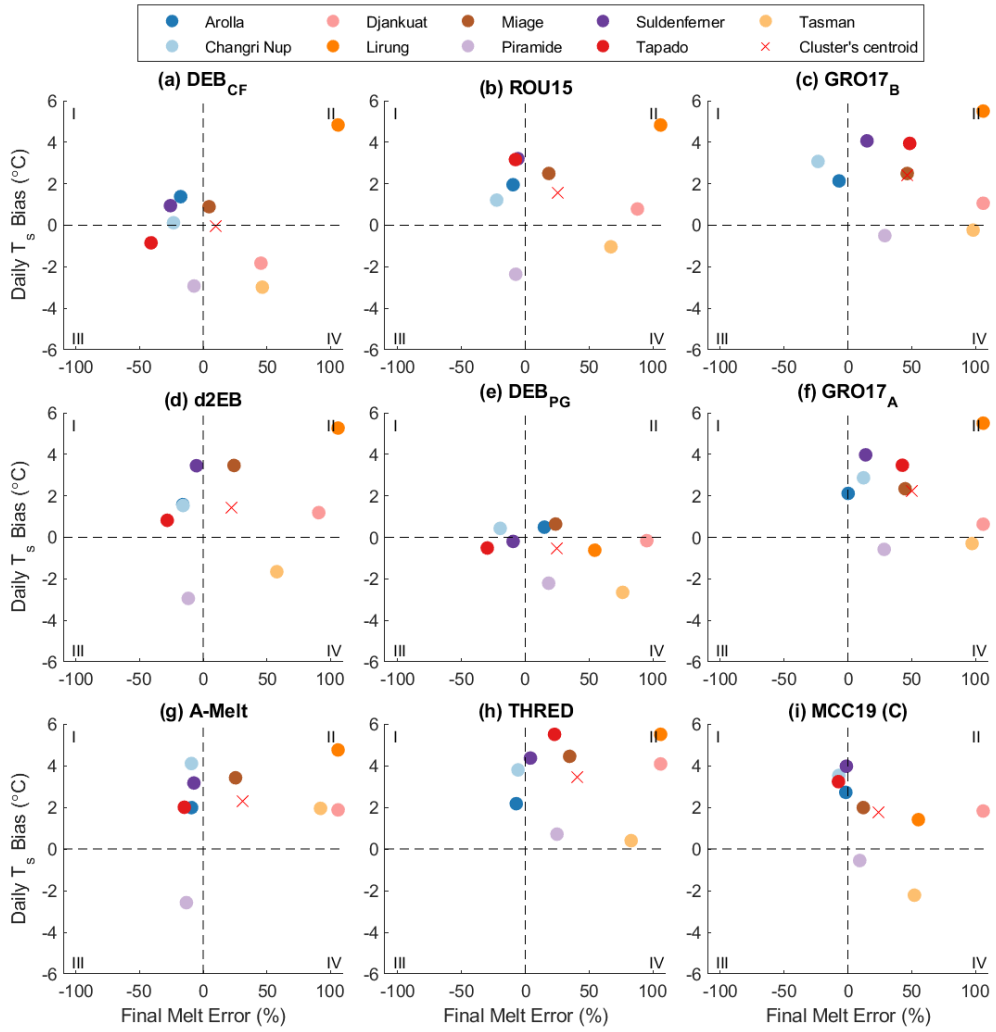

Figure S4. Consistency of model performance across the two validation datasets. For each model (a-i), each site is scattered based on their daily temperature bias and melt error. Dashed lines correspond to the zero line for both axes, and separate the plot in four quadrants. Quadrants above the horizontal dashed line indicate overestimation of surface temperature. Quadrants to the right of the vertical dashed line indicate overestimation of melt. Values higher or lower than the axes limit are shown on the axis limit.

3.2. Individual model performance

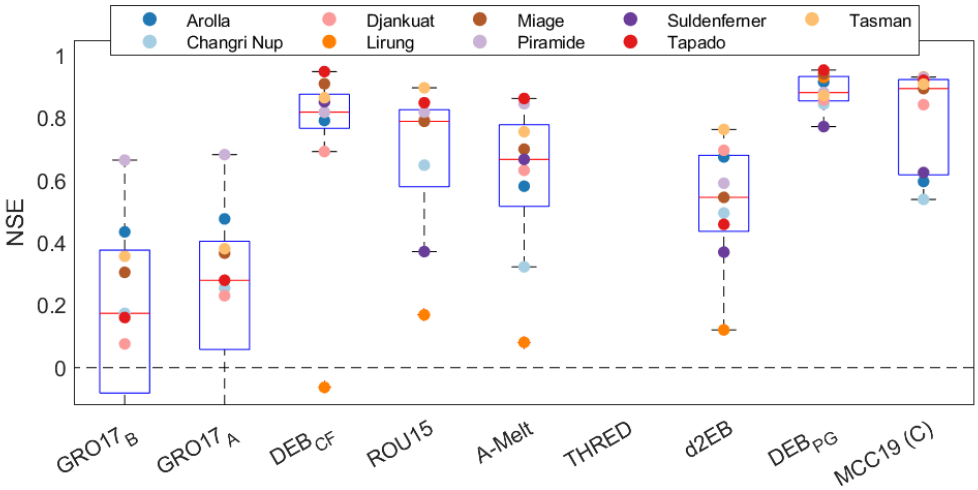

Figure S5. Validation of the energy balance model simulations against surface temperature, at all sites. Statistical boxes for each model show the distribution of the Nash Sutcliffe Efficiency of surface temperature at each site. Note that the THRED model is run at daily resolution and therefore is not validated with NSE as discussed in the text. GRO17$_A$ and GRO17$_B$ are

negative at Lirung (-4.1 and -3.4, respectively) and Suldenferner (-0.55 and -0.46, respectively) but are not displayed for better visibility of the plot.

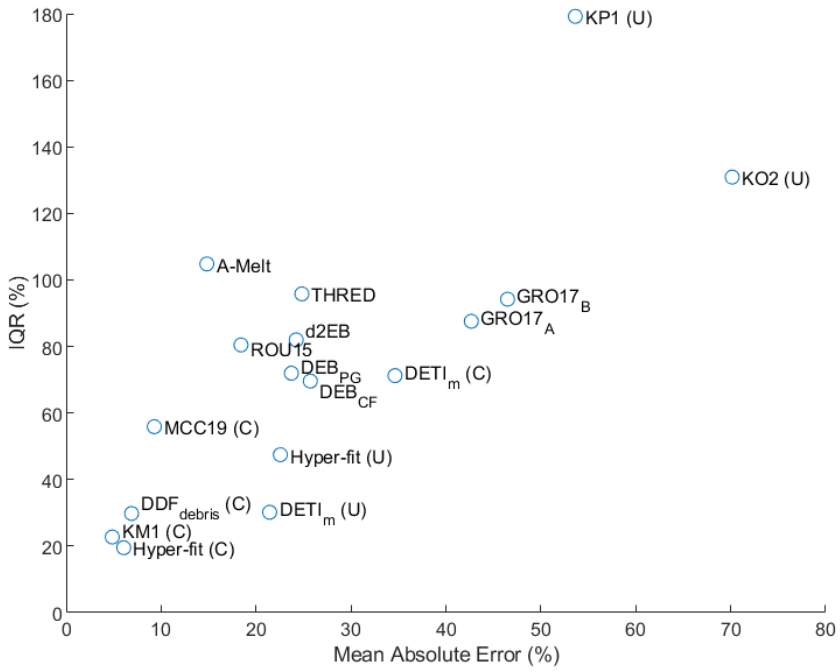

Figure S6. Alternative visualization for the model ranking of Table 4.

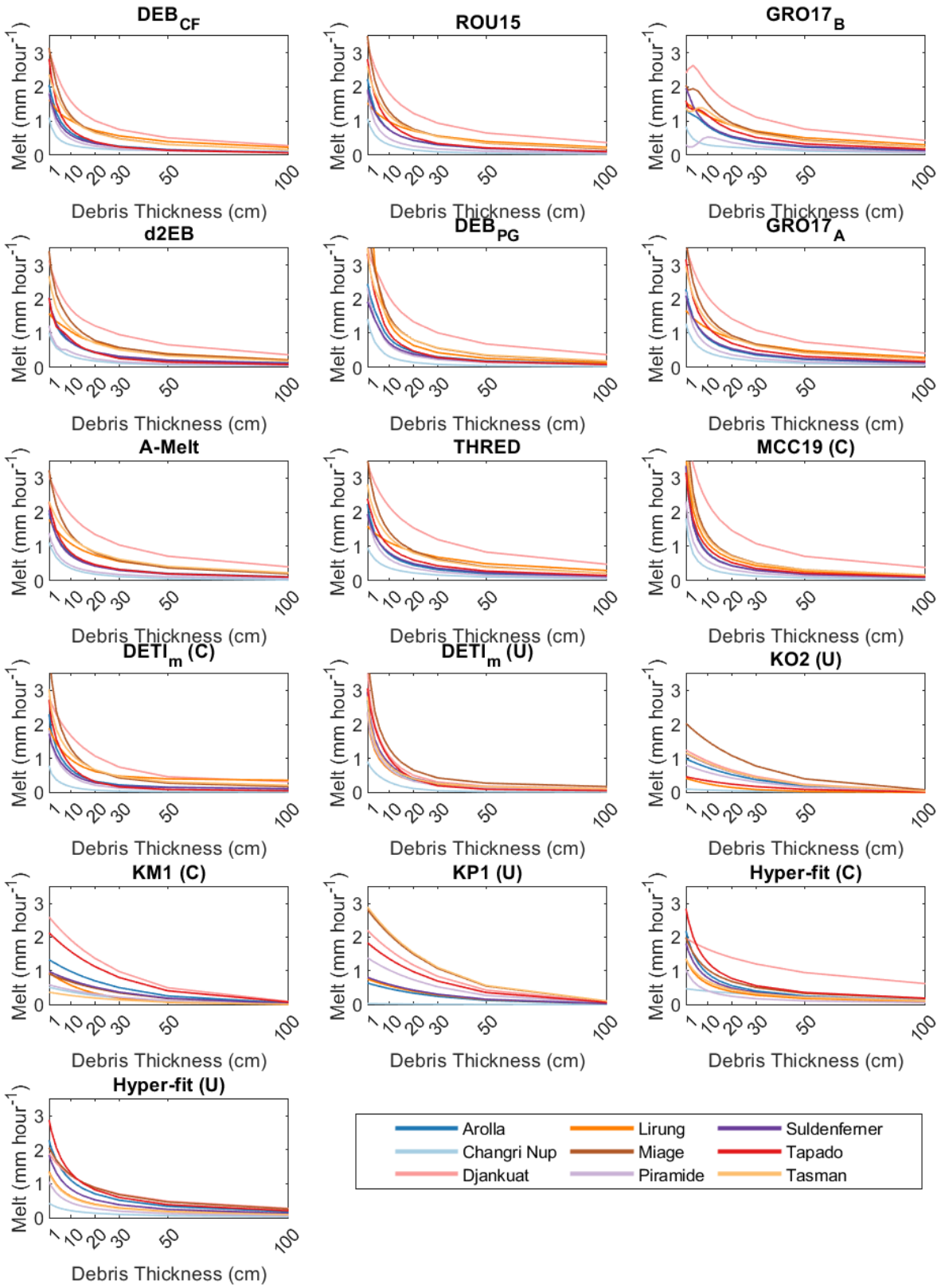

Figure S7. Østrem curves for each model at all sites.

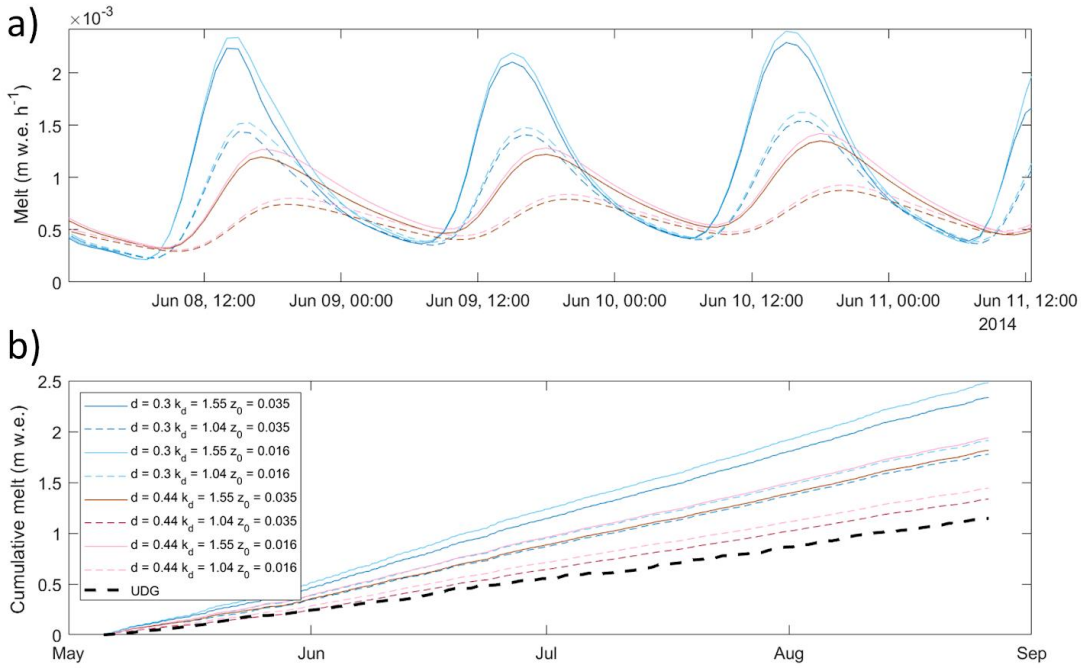

Figure S8. Melt rates simulated by the DEB_{CF} model at Lirung, with debris thickness (d) = 30 cm (thickness at the AWS location) and d = 44 cm (thickness at the UDG location), and with debris conductivity and surface roughness from Lirung (k = 1.55 and z_0 = 0.035) and Miage (k = 1.04 and z_0 = 0.016) as well as combinations of them. Panel a) shows hourly melt for three days of the simulation period, b) shows the cumulative melt of all scenarios compared to the UDG record.

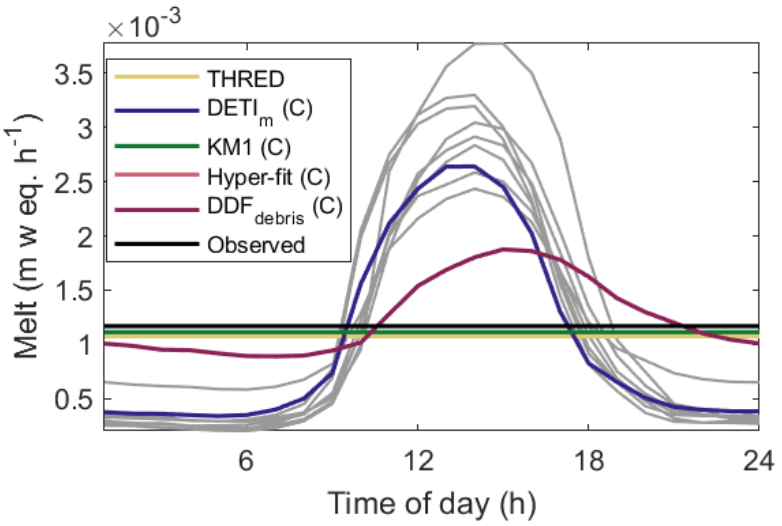

Figure S9. Illustrations of the temporal sub-daily cycle of melt of energy balance (and simplified energy balance) models (in grey) versus simple temperature index approaches (coloured), for one study site, Arolla (debris thickness = 6 cm). The cross (x) indicates the observed daily melt at the site. Daily melt simulated by the models operating at the daily time step are also indicated to show that daily values arise from overestimation of melt at night and underestimation of melt during the day (relative to the energy-balance models operating at hourly resolution). Hyper-fit and DDF_{debris} overlap each other.

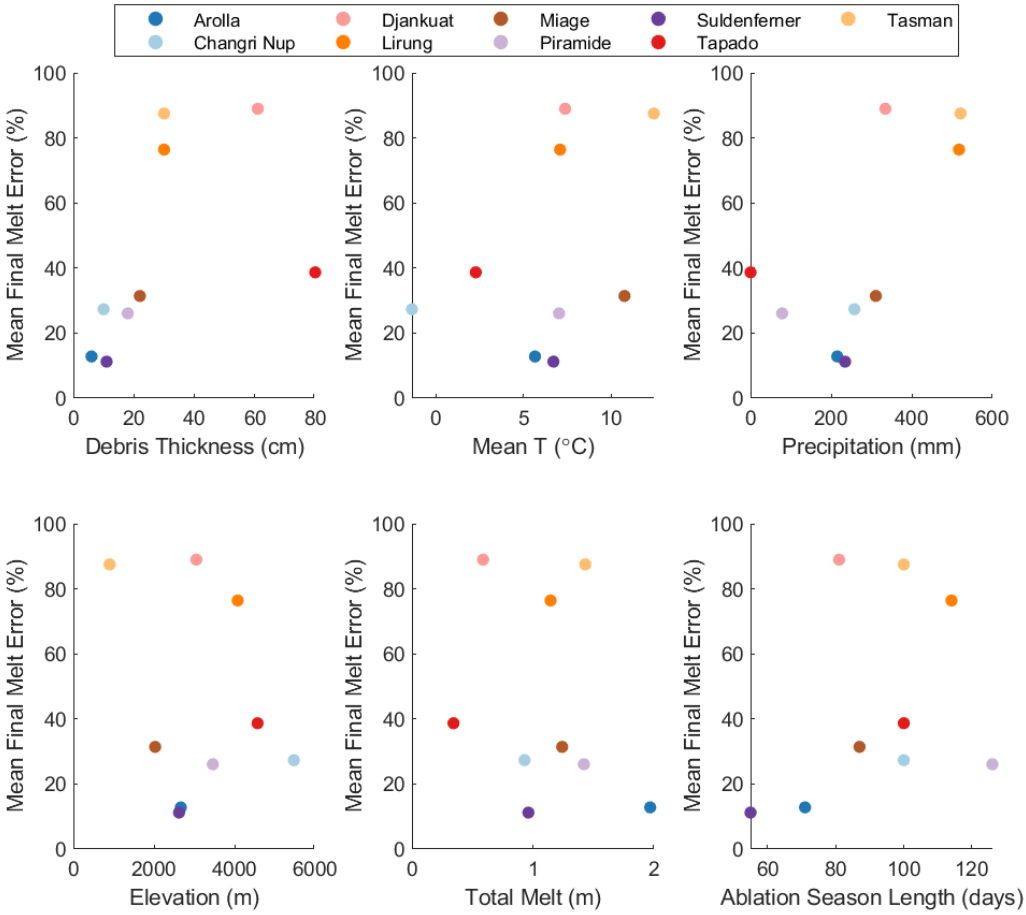

Figure S10. Mean melt error against site characteristics. For each of: debris thickness, mean air temperature, total precipitation, elevation, total melt, and simulation period length, the mean absolute error of the ensemble of models at each site is shown.

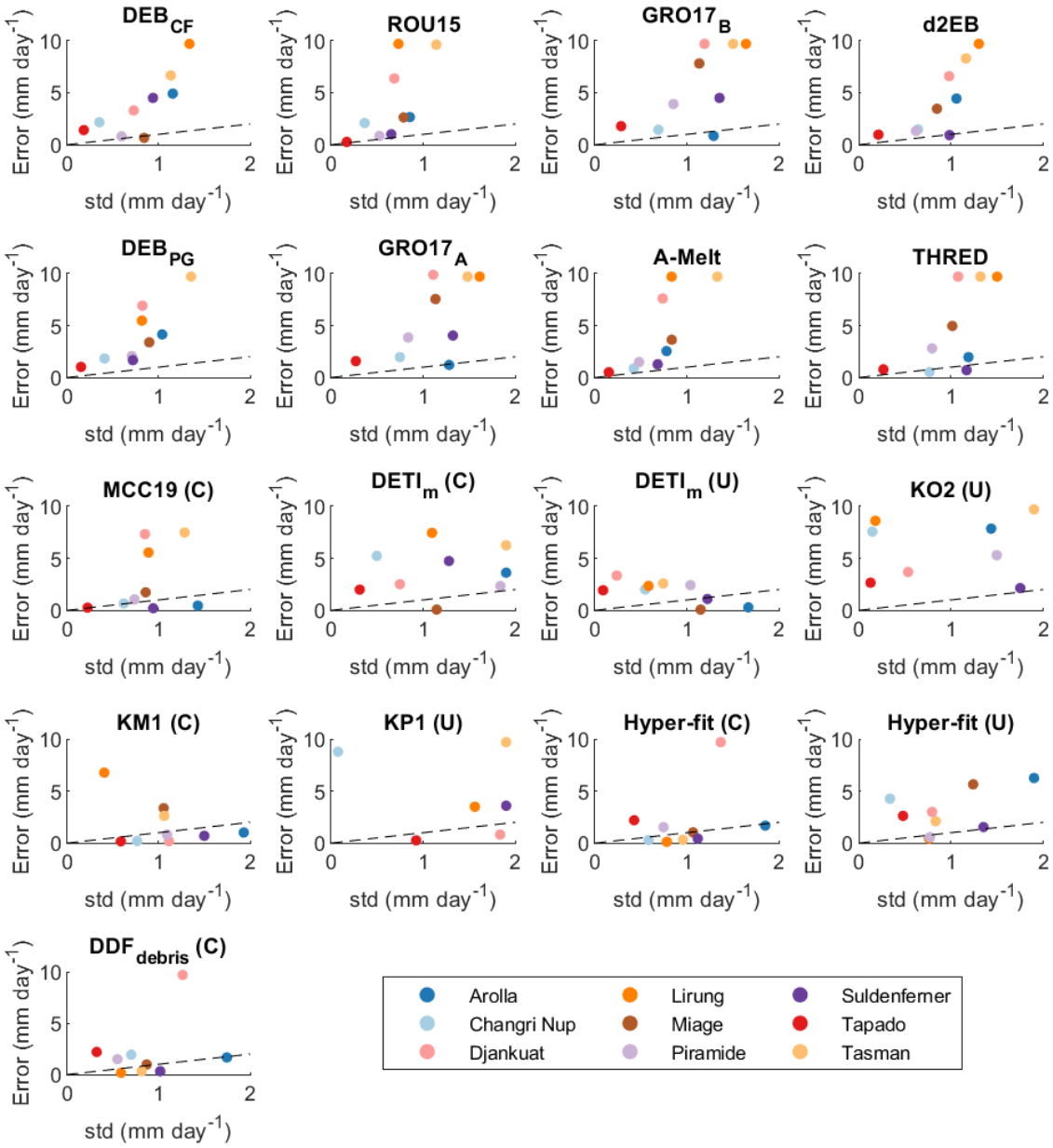

Figure S11. Modelled melt error (y-axis) vs model uncertainty (assumed equal to the standard deviation of the Monte Carlo simulations, x-axis). Dashed line is the 1:1 line, so wherever a point is above the line, it means the error is larger than the Monte Carlo Uncertainty.

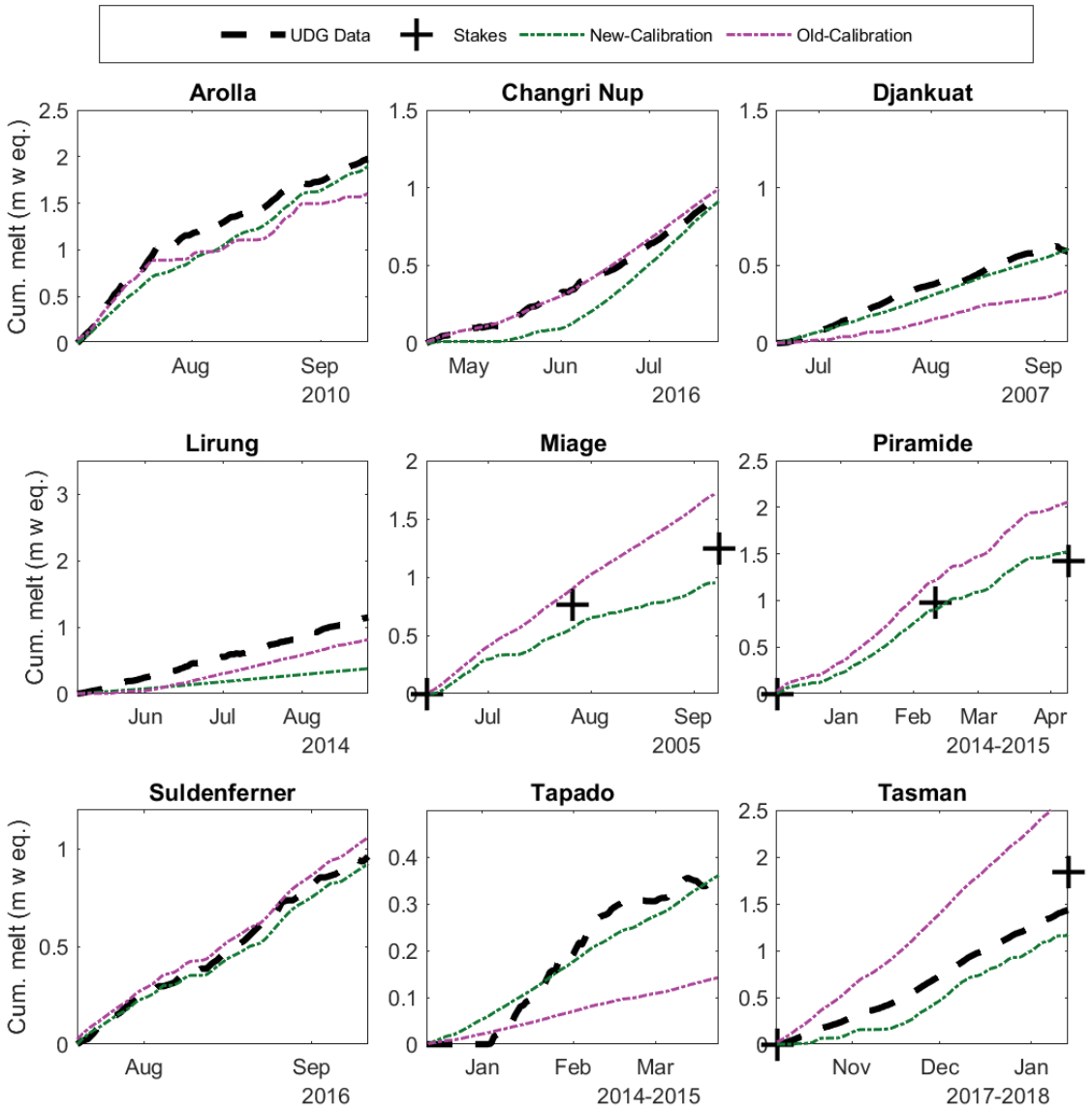

Figure S12. Melt simulations from KM1 model, new versus old calibration scheme: In the new calibration, the calibration strategy is set up to match the total final melt, and in the old calibration, to match mean daily melt rates.

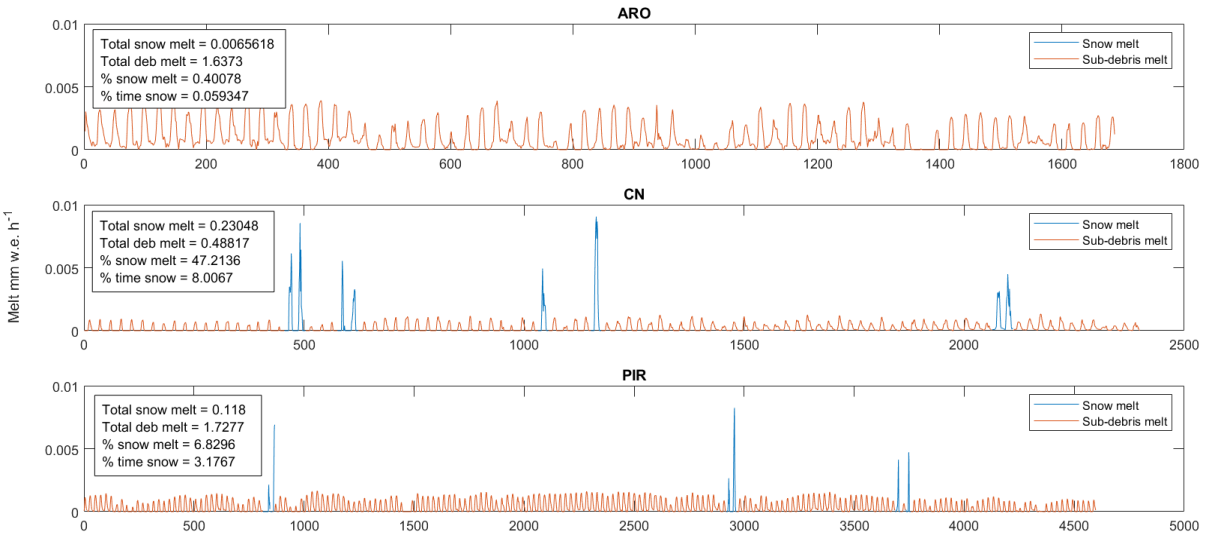

Figure S13. Snowmelt calculated by the DEB_{CF} model at the three sites where occasional snowfalls occurred during the period of record selected for this intercomparison.

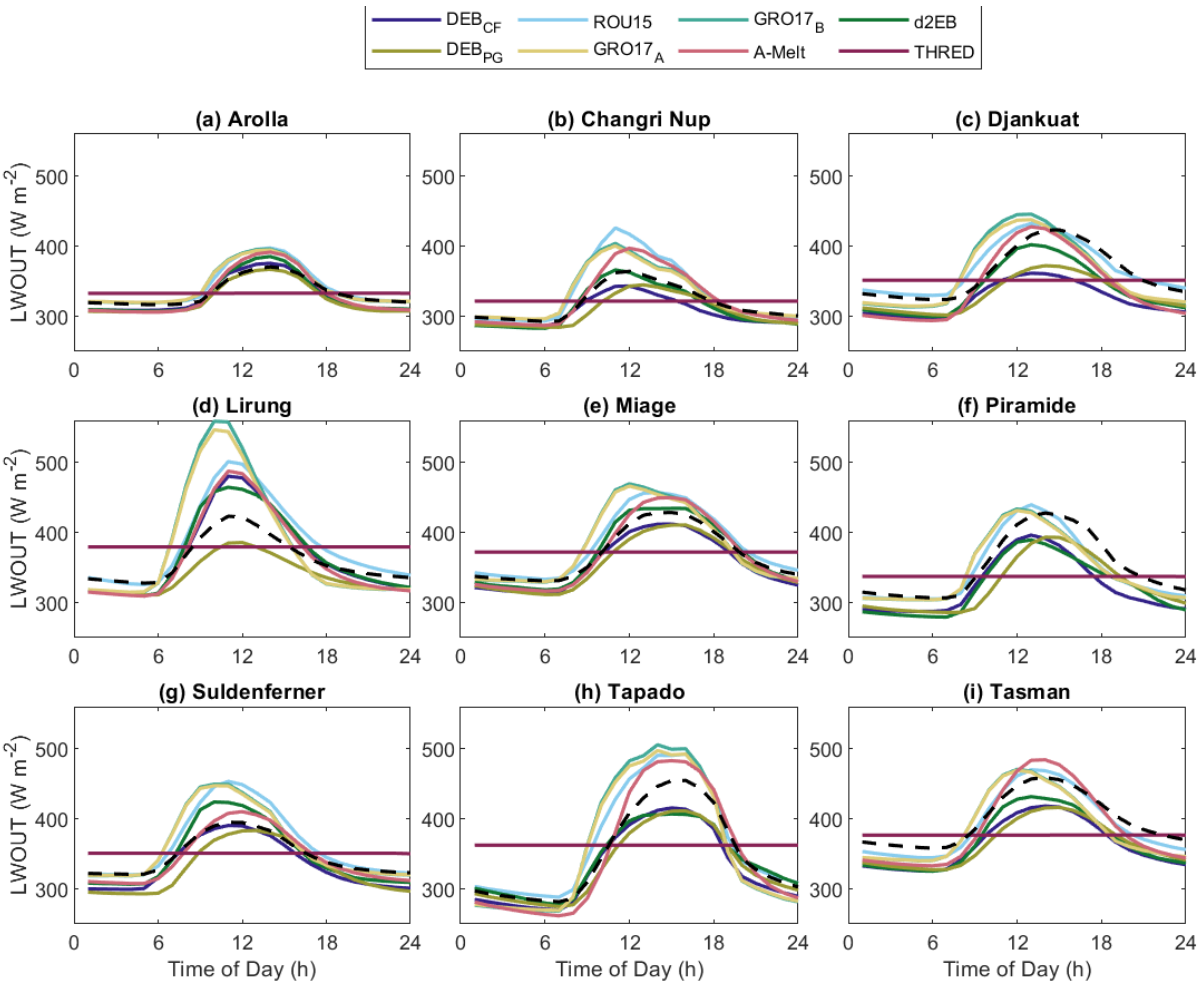

Figure S14. Outgoing longwave radiation flux (LW_{out}) computed by each model, from the internally simulated debris surface temperature. The dashed black line is the observed LW_{out} from the sensor. Notice that $GRO17_A$ and $GRO17_B$ overlap each other.

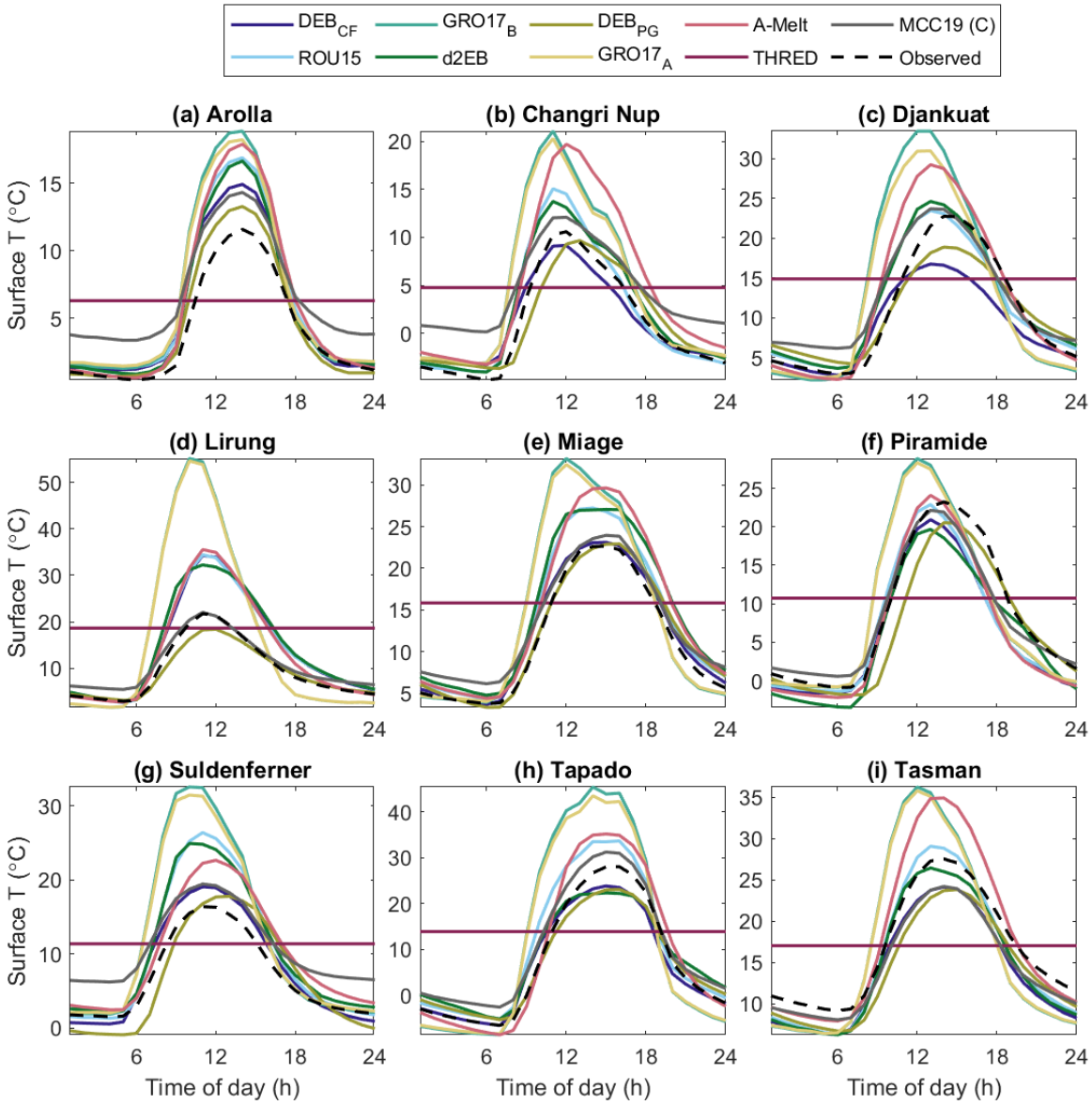

Figure S15. Mean daily cycle of debris surface temperature computed by each model at each site. All models simulate surface temperature internally.

Table S28. Average daily energy fluxes simulated by the models at Arolla, Changri Nup, and Djankuat, during the period of simulation. L↑ is the outgoing longwave radiation flux. H is sensible heat flux. LE latent heat flux. G is ground heat flux. P is precipitation flux. All fluxes in $W\ m^{-2}$.

Glacier	Model	L↑	H	LE	G	P
Arolla	$GRO17_A$	342.48	-13.53	-7.98	103.31	-
	$GRO17_B$	342.39	-13.97	-	102.86	-
	DEB_{CF}	329.17	-35.02	-3.56	-	0.12
	ROU15	342.91	-12.75	-3.18	-96.85	0.13
	A-Melt	332.35	-5.63	-17.46	-	-
	d2EB	332.86	-19.17	-0.38	101.14	-
	THRED	330.23	-1.65	-33.20	-	-
	DEB_{PG}	324.81	-12.12	0.00	-114.10	-
	MCC19	334.11	-	-	-	-
Changri Nup	$GRO17_A$	331.59	-82.29	-29.85	40.86	-
	$GRO17_B$	330.68	-84.64	-	39.40	-
	DEB_{CF}	305.97	-91.21	-35.07	-	-0.11
	ROU15	334.67	-62.29	-28.10	-15.31	-0.19
	A-Melt	325.28	-49.10	-29.27	-	-
	d2EB	321.56	-88.19	0.00	34.08	-
	THRED	312.71	-33.97	-85.42	-	-
	DEB_{PG}	306.88	-113.82	0.00	-14.44	-
	MCC19	319.14	-	-	-	-
Djankuat	$GRO17_A$	362.48	-104.26	0.00	56.39	-
	$GRO17_B$	360.69	-108.02	-	54.28	-
	DEB_{CF}	324.08	-81.01	-74.99	-	-0.04
	ROU15	369.58	-94.94	-2.44	-53.49	-0.30
	A-Melt	343.52	-53.69	-65.23	-	-
	d2EB	351.50	-102.49	0.00	68.41	-
	THRED	339.22	-59.95	-59.94	-	-
	DEB_{PG}	331.50	-118.99	0.00	-57.89	-
	MCC19	362.24	-	-	-	-

Table S29. Average daily energy fluxes simulated by the models at Lirung, Miage and Piramide, during the period of simulation. L↑ is the outgoing longwave radiation flux. H is sensible heat flux. LE latent heat flux. G is ground heat flux. P is precipitation flux. All fluxes in $W\ m^{-2}$.

Glacier	Model	L↑	H	LE	G	P
Lirung	$GRO17_A$	383.01	-31.26	0.00	84.39	-
	$GRO17_B$	380.45	-36.85	-	81.09	-
	DEB_{CF}	367.93	-44.27	-3.68	-	-0.40
	ROU15	386.36	-31.13	-2.65	-73.28	-0.34
	Λ-Melt	366.31	-29.64	-23.04	-	-
	d2EB	379.53	-28.45	0.00	89.10	-
	THRED	369.12	-17.34	-6.35	-	-
	DEB_{PG}	338.42	-99.07	0.00	-53.69	-
	MCC19	360.95	-	-	-	-
Miage	$GRO17_A$	381.38	-68.05	0.00	73.32	-
	$GRO17_B$	380.65	-69.57	-	72.49	-
	DEB_{CF}	355.83	-92.21	-13.50	-	0.02
	ROU15	383.52	-59.81	-12.29	-65.73	-0.04
	Λ-Melt	369.58	-36.13	-45.66	-	-
	d2EB	372.19	-75.07	0.00	74.90	-
	THRED	369.71	-55.01	-28.73	-	-
	DEB_{PG}	354.41	-91.23	0.00	-65.60	-
	MCC19	369.54	-	-	-	-
Piramide	$GRO17_A$	347.59	-85.50	-0.30	47.63	-
	$GRO17_B$	347.24	-86.25	-	47.09	-
	DEB_{CF}	323.68	-83.05	-37.03	-	0.05
	ROU15	348.06	-51.87	-41.89	-34.21	0.05
	Λ-Melt	0.00	-20.75	-94.55	-	-
	d2EB	337.26	-89.65	-0.92	48.34	-
	THRED	323.09	-16.03	-156.86	-	-
	DEB_{PG}	325.80	-98.58	0.00	-41.36	-
	MCC19	352.75	-	-	-	-

Table S30. Average daily energy fluxes simulated by the models at Suldenferner, Tapado and Tasman, during the period of simulation. L↑ is the outgoing longwave radiation flux. H is sensible heat flux. LE latent heat flux. G is ground heat flux. P is precipitation flux. All fluxes in $W\ m^{-2}$.

Glacier	Model	L↑	H	LE	G	P
Suldenferner	$GRO17_A$	362.85	-30.61	0.00	72.11	-
	$GRO17_B$	362.45	-31.62	-	71.45	-
	DEB_{CF}	334.55	-73.23	-3.68	-	-0.08
	ROU15	365.24	-30.33	-3.00	-64.99	-0.06
	Λ-Melt	345.45	-26.40	-27.03	-	-
	d2EB	350.75	-38.43	0.06	72.33	-
	THRED	347.67	-30.18	-22.69	-	-
	DEB_{PG}	329.17	-64.80	0.00	-56.15	-
	MCC19	347.62	-	-	-	-
Tapado	$GRO17_A$	360.30	-165.68	0.00	17.93	-
	$GRO17_B$	358.27	-168.27	-	17.24	-
	DEB_{CF}	330.72	-200.47	0.00	-	0.00
	ROU15	367.57	-158.29	0.00	-13.71	0.00
	Λ-Melt	348.30	-75.77	-103.78	-	-
	d2EB	362.46	-164.41	0.00	16.49	-
	THRED	339.74	-81.81	-157.93	-	-
	DEB_{PG}	331.81	-190.80	0.00	-11.20	-
	MCC19	349.09	-	-	-	-
Tasman	$GRO17_A$	386.28	-65.56	0.00	97.70	-
	$GRO17_B$	386.06	-66.09	-	97.38	-
	DEB_{CF}	363.10	-87.10	-14.82	-	0.29
	ROU15	392.19	-50.48	-13.64	-91.83	0.36
	Λ-Melt	388.14	-44.98	-78.49	-	-
	d2EB	376.79	-71.07	-0.01	100.05	-
	THRED	368.63	-31.66	-62.07	-	-
	DEB_{PG}	364.19	-81.49	0.00	-95.02	-
	MCC19	397.90	-	-	-	-

References

Anderson, L. S. and Anderson, R. S.: Modeling debris-covered glaciers: Response to steady debris deposition, The Cryosphere, 10, 1105–1124, doi:10.5194/tc-10-1105-2016, 2016.

Ayala, A., Pellicciotti, F., MacDonell, S., McPhee, J., and Burlando, P.: Patterns of glacier ablation across N orth- C entral C hile: Identifying the limits of empirical melt models under sublimation-favorable conditions, Water Resour. Res., 53, 5601–5625, doi:10.1002/2016WR020126, 2017.

Ayala, A., Pellicciotti, F., MacDonell, S., McPhee, J., Vivero, S., Campos, C., and Egli, P.: Modelling the hydrological response of debris-free and debris-covered glaciers to present climatic conditions in the semiarid Andes of central Chile, Hydrol. Process., 30, 4036–4058, doi:10.1002/hyp.10971, 2016.

Bozhinskiy, A. N., Krass, M. S., and Popovnin, V. V.: Role of Debris Cover in the Thermal Physics of Glaciers, J. Glaciol., 32, 255–266, doi:10.3189/S0022143000015598, 1986.

Brock, B. W., Mihalcea, C., Kirkbride, M. P., Diolaiuti, G., Cutler, M. E. J., and Smiraglia, C.: Meteorology and surface energy fluxes in the 2005–2007 ablation seasons at the Miage debris-covered glacier, Mont Blanc Massif, Italian Alps, J. Geophys. Res. Atmos., 115, 2009JD013224, doi:10.1029/2009JD013224, 2010.

Carenzo, M., Pellicciotti, F., Mabillard, J., Reid, T., and Brock, B. W.: An enhanced temperature index model for debris-covered glaciers accounting for thickness effect, Adv. Water Resour., 94, 457–469, doi:10.1016/j.advwatres.2016.05.001, 2016.

Chand, M. B. and Kayastha, R. B.: Study of thermal properties of supraglacial debris and degree-day factors on Lirung Glacier, Nepal, Sci. Cold Arid Reg., 10, 357–368, doi:10.3724/SP.J.1226.2018.00357, 2018.

Elagina, N., Rets, E., Korneva, I., Toropov, P., and Lavrentiev, I.: Simulation of mass balance and glacial runoff of Mount Elbrus from 1984 to 2022, Hydrol. Sci. J., doi:10.1080/02626667.2025.2516080, 2025.

Evatt, G. W., Abrahams, I. D., Heil, M., Mayer, C., Kingslake, J., Mitchell, S. L., Fowler, A. C., and Clark, C. D.: Glacial melt under a porous debris layer, J. Glaciol., 61, 825–836, doi:10.3189/2015JoG14J235, 2015.

Fujita, K. and Sakai, A.: Modelling runoff from a Himalayan debris-covered glacier, Hydrol. Earth Syst. Sci., 18, 2679–2694, doi:10.5194/hess-18-2679-2014, 2014.

Fyffe, C. L., Reid, T. D., Brock, B. W., Kirkbride, M. P., Diolaiuti, G., Smiraglia, C., and Diotri, F.: A distributed energy-balance melt model of an alpine debris-covered glacier, J. Glaciol., 60, 587–602, doi:10.3189/2014JoG13J148, 2014.

Groos, A. R. and Mayer, C.: glacierSMBM: Glacier Surface Mass Balance Model, R package (v0.1), https://CRAN.R-project.org/package=glacierSMBM, 2017.

Groos, A. R., Mayer, C., Smiraglia, C., Diolaiuti, G., and Lambrecht, A.: A first attempt to model region-wide glacier surface mass balances in the Karakoram: Findings and future challenges, Geogr. Fis. Dinam. Quat., 40, 137–159, doi:10.4461/GFDQ.2017.40.10, 2017.

Hock, R.: Temperature index melt modelling in mountain areas, J. Hydrol., 282, 104–115, doi:10.1016/S0022-1694(03)00257-9, 2003.

Kayastha, R. B., Takeuchi, Y., Nakawo, M., and Ageta, Y.: Practical prediction of ice melting beneath various thickness of debris cover on Khumbu Glacier, Nepal, using a positive degree-day factor, 264, 71–81, 2000.

Kirkbride, M.: Ice Flow Vectors on the Debris-Mantled Tasman Glacier, 1957–1986, Geogr. Ann. A. Phys. Geogr., 77, 147–157, doi:10.1080/04353676.1995.11880435, 1995.

Kuzmin, P. P.: The Process of Snow Melting, Leningrad: Gidrometizdat, 1961.

Lambrecht, A., Mayer, C., Hagg, W., Popovnin, V., Rezepkin, A., Lomidze, N., and Svanadze, D.: A comparison of glacier melt on debris-covered glaciers in the northern and southern Caucasus, The Cryosphere, 5, 525–538, doi:10.5194/tc-5-525-2011, 2011.

Lejeune, Y., Bertrand, J.-M., Wagnon, P., and Morin, S.: A physically based model of the year-round surface energy and mass balance of debris-covered glaciers, J. Glaciol., 59, 327–344, doi:10.3189/2013JoG12J149, 2013.

McCarthy, M. J.: Quantifying supraglacial debris thickness at local to regional scales, https://doi.org/10.17863/CAM.41172, 2018.

McCarthy, M.: A simplified energy-balance model for ice melt below debris (Version 1.0.0), GitHub, https://github.com/mchl-mccrthy/seb_model, 2025.

McPhee, J., MacDonnel, S., & Shaw, T.: 6_Pirámide Data [Data set]. Zenodo. https://doi.org/10.5281/zenodo.3056072, 2019.

Miles, E. S., Steiner, J. F., and Brun, F.: Highly variable aerodynamic roughness length (z0) for a hummocky debris-covered glacier, J. Geophys. Res. Atmos., 122, 8447–8466, doi:10.1002/2017JD026510, 2017.

Nicholson, L. and Benn, D. I.: Calculating ice melt beneath a debris layer using meteorological data, J. Glaciol., 52, 463–470, doi:10.3189/172756506781828584, 2006.

Oerlemans, J.: Glaciers and Climate Change, A.A. Balkema Publishers, 2001.

Pellicciotti, F., Brock, B., Strasser, U., Burlando, P., Funk, M., and Corripio, J.: An enhanced temperature-index glacier melt model including the shortwave radiation balance: Development and testing for Haut Glacier d'Arolla, Switzerland, J. Glaciol., 51, 573–587, doi:10.3189/172756505781829124, 2005.

Reid, T. D. and Brock, B. W.: An energy-balance model for debris-covered glaciers including heat conduction through the debris layer, J. Glaciol., 56, 903–916, doi:10.3189/002214310794457218, 2010.

Reid, T. D., Carenzo, M., Pellicciotti, F., and Brock, B. W.: Including debris cover effects in a distributed model of glacier ablation, J. Geophys. Res. Atmos., 117, 2012JD017795, doi:10.1029/2012JD017795, 2012.

Rets, E. and Kireeva, M.: Hazardous hydrological processes in mountainous areas under the impact of recent climate change: Case study of Terek River basin, 340, 126–134, 2010.

Robertson, E. C.: General and Engineering Geology of the Northern Part of Pueblo, Colorado (Open-File Report 88–441), U.S. Geological Survey, https://pubs.usgs.gov/of/1988/0441/report.pdf, 1988.

Röhl, K.: Characteristics and evolution of supraglacial ponds on debris-covered Tasman Glacier, New Zealand, J. Glaciol., 54, 867–880, doi:10.3189/002214308787779861, 2008.

Rounce, D. R., Quincey, D. J., and McKinney, D. C.: Debris-covered glacier energy balance model for Imja–Lhotse Shar Glacier in the Everest region of Nepal, The Cryosphere, 9, 2295–2310, doi:10.5194/tc-9-2295-2015, 2015.

Rye, C. J., Arnold, N. S., Willis, I. C., and Kohler, J.: Modeling the surface mass balance of a high Arctic glacier using the ERA-40 reanalysis, J. Geophys. Res. Earth Surf., 115, 2009JF001364, doi:10.1029/2009JF001364, 2010.

Steiner, J. F., Kraaijenbrink, P. D. A., and Immerzeel, W. W.: Distributed Melt on a Debris-Covered Glacier: Field Observations and Melt Modeling on the Lirung Glacier in the Himalaya, Front. Earth Sci., 9, 678375, doi:10.3389/feart.2021.678375, 2021.

Steiner, J. F., Litt, M., Stigter, E. E., Shea, J., Bierkens, M. F. P., and Immerzeel, W. W.: The Importance of Turbulent Fluxes in the Surface Energy Balance of a Debris-Covered Glacier in the Himalayas, Front. Earth Sci., 6, 144, doi:10.3389/feart.2018.00144, 2018.

Sturm, M., Holmgren, J., König, M., and Morris, K.: The thermal conductivity of seasonal snow, J. Glaciol., 43, 26–41, doi:10.3189/S0022143000002781, 1997.

Wagnon, P.: 2_Changri Nup Data [Dataset], https://doi.org/10.5281/ZENODO.3048780, 2019.

Winter-Billington, A., Moore, R. D., and Dadic, R.: Evaluating the transferability of empirical models of debris-covered glacier melt, J. Glaciol., 66, 978–995, doi:10.1017/jog.2020.57, 2020.